


## Corrosion and wear behavior of slag cleaning chain and influence of Cr, Ni and Mo under different chloride ion concentration

Jintao Bai<sup>1</sup>, Xiaohan Ma<sup>1</sup>, Shengxing Wang<sup>1</sup>, Jun Niu<sup>1</sup>, Ruina Ma<sup>1,2</sup>,  
An Du<sup>1,2</sup>, Xue Zhao<sup>1,2</sup>, Yongzhe Fan<sup>2,3</sup> 

<sup>1</sup>Hebei University of Technology, Tianjin, China.

<sup>2</sup>Hebei Key Laboratory of New Functional Materials, Tianjin, China.

<sup>3</sup>Hebei University of Technology, School of Materials Science and Engineering, Tianjin, China.

e-mail: b15128006585@163.com, 18239339152@163.com, 202211801004@stu.hebut.edu.cn, nj1367439016@163.com, maryna@126.com, duan@hebut.edu.cn, zhaoxue@hebut.edu.cn, fyz@hebut.edu.cn

### ABSTRACT

To address the issue of corrosive wear resulting from the addition of desulphurization wastewater into the wet slag removal system, this study investigated the corrosive wear behavior of chain steel (specifically 17NiCrMo6 steel) in desulphurization wastewater with varying chloride concentrations. Weight loss, micro-phase characterization, and electrochemical testing methods were employed for analysis. The findings indicate that as the chloride concentration increases, the weight loss rates for both pure corrosion and corrosive wear exhibit a pattern of initial increase, followed by a decrease, and then another increase. This trend can be attributed to the fact that as the chloride concentration rises, the corrosion products become denser, thereby increasing the difficulty of the corrosion reaction.

**Keywords:** Corrosive wear; Corrosion mechanism; Corrosion-resistant elements; Electrochemical test.

### 1. INTRODUCTION

The pollution-free discharge of industrial wastewater poses a significant challenge for coal-fired power plants. The technology typically employed for treating high-salinity wastewater (such as desulphurization wastewater) in these plants does not currently meet environmental protection requirements due to its complex process chain and the high costs associated with chemical treatment and machine maintenance [1]. However, the use of desulphurization wastewater as a cooling circulating water for coal power plant slag machines has gained attention due to its simple treatment method and low cost. Nevertheless, the harsh operating environment of the wet slag removal system and the corrosive effects resulting from the introduction of high-salt wastewater give rise to new corrosion issues for the key components of the slag extraction machine [2]. Since the chain is the connecting part of the sprocket that drives and pulls the scraper, if the chain is not working properly, the entire wet slag removal system will be paralyzed., is typically made of 17NiCrMo6 steel. Understanding the mechanisms of corrosion and wear of the chain in this new environment will provide a theoretical basis for evaluating the feasibility of using desulphurization wastewater as the cooling water for the slag extraction machine.

There have been numerous studies conducted on the impact of desulfurization wastewater added to the wet slag removal system. For instance, LIN *et al.* [2] conducted research on the corrosion behavior of key materials in the system. They comprehensively examined the effects of temperature, pH, and electrical conductivity on the system and found that the corrosion rate of 1Cr18Ni9Ti steel and 304 stainless steel is lower than 0.1 mm/y. These materials can withstand operation in this environment. However, the corrosion rate of T12 steel, 65Mn steel, and 20CrMnTi steel is higher than 1.0 mm/y, making them unsuitable for long-term operation in this environment. ZOU [3] studied the impact of introducing desulphurization wastewater into the slag water system. The results showed that this would not have a significant impact on the overall water quality and would not cause the recovered residue to exceed toxic discharge standards. However, none of these studies systematically investigated the corrosion mechanism of a specific key component.

The potential corrosiveness of desulphurization wastewater mainly stems from its high concentration of Cl<sup>-</sup>. Therefore, it is necessary to examine the corrosion effects of different concentrations of Cl<sup>-</sup> on key

components after adding it to the slag water system. Some studies [4–6] have indicated that the corrosion rate of carbon steel gradually increases with increasing  $\text{Cl}^-$  concentration, reaching a peak before gradually decreasing. The corrosion products also change with the increase in  $\text{Cl}^-$  concentration. The unstable  $\gamma\text{-FeOOH}$  and  $\beta\text{-FeOOH}$  transform into the more stable  $\alpha\text{-FeOOH}$  structure, resulting in a denser corrosion product film and increased thickness. GOYAL *et al.* [5] showed that a dense structure helps improve the corrosion resistance of steel. The morphology of these corrosion products varies, and with higher  $\text{Cl}^-$  concentrations, both general corrosion and pitting corrosion occur. DONG *et al.* [6] investigated the role of various corrosion-resistant elements in corrosion, metal cations such as  $\text{Ni}^{2+}$ ,  $\text{Mo}^{4+}$ ,  $\text{Mo}^{6+}$ , and other metal cations can be absorbed by electronegative oxides, leading to the formation of corresponding compounds. These compounds also possess electronegative properties, which further attract  $\text{Mo}^{4+}$  and  $\text{Mo}^{6+}$  to form metal oxides. The synergistic effect of these oxides weakens the erosion of  $\text{Cl}^-$  on carbon steel. SAHIL *et al.* [7] sprayed  $\text{Cr}_2\text{O}_3$ -wt%  $\text{TiO}_2$  on the surface of ASME-SA213-T-22 boiler steel with 10% and 20%  $\text{TiO}_2$  in  $\text{Cr}_2\text{O}_3$  matrix. And the corrosion resistance of the coatings was evaluated in a molten salt environment of 40wt%  $\text{Na}_2\text{SO}_4$ -60wt%  $\text{V}_2\text{O}_5$ . The experimental results showed that the increase in  $\text{TiO}_2$  content resulted in a greater decrease in corrosion rate relative to the bare steel corrosion rate, from 84.14% to 86.20%. The XRD results indicate that  $\text{TiO}_2$  and  $\text{TiO}_3$  are the main protective oxide layers. However, these studies have not considered the impact of  $\text{Cl}^-$  on wear.

Some studies [8, 9] have shown that the addition of other factors in the environment (e.g., solid particles, suspended ions, solution flow rate, etc.) can cause corrosion to become more severe. During the operation of the slag extraction machine, the impact of the slag on the chain can cause mechanical losses. These affected areas become vulnerable to  $\text{Cl}^-$  erosion, resulting in more severe corrosion. CHEN *et al.* [10] have pointed out that as the  $\text{Cl}^-$  content in the solution increases, the electrical conductivity also increases. This leads to the rapid removal of the metal's passivation film under corrosion wear, intensifying the corrosion wear. SMITH *et al.* [11] have studied the influence of salinity on engineering structural steels. They have explored the response of different types of steels to various salt concentrations. Erosion-corrosion tests were conducted on a recirculating submerged impingement slurry jet test-rig (FEC) to observe the damage to the samples from the suspensions at three different concentrations of 0.05% NaCl, 3.5% NaCl, and 10% NaCl, and to evaluate the damage to the impact zone of the samples using total volumetric loss and volumetric analysis techniques. These samples were acid washed after the FEC tests to remove the surface corrosion products. Additionally, comparative observations of the effects on the steel structure (martensite, austenite, and biphasic) of three grades of stainless steel were included.

In summary, extensive studies have shown that the concentration of  $\text{Cl}^-$  has some effect on corrosive wear. However, there is limited research on the mechanism involved, and most studies neglect the role of corrosion-resistant elements. Therefore, a detailed study on the effect of  $\text{Cl}^-$  concentration on corrosive wear and an in-depth investigation of its mechanism will provide a theoretical basis for the effective protection of chain steel.

The objective of this study is to investigate the chloride ( $\text{Cl}^-$ ) tolerance range of chain steel and its impact on corrosive wear. The specimens were subjected to erosion experiments using hanging chip experiments and the post-experiment specimens were analytically characterized. The behavior and role of three elements, chromium (Cr), nickel (Ni), and molybdenum (Mo), contained in 17NiCrMo6 steel were investigated because  $\text{Cl}^-$  affects the content of alloying elements in the corrosion products and the physical phase structure. The weight loss rate was calculated to evaluate the wear resistance and corrosion resistance. The surface roughness of corroded samples was analyzed using an Olympus microscope. The surface morphology, cross-section morphology, and element distribution of the rust layer were characterized using a scanning electron microscope and energy dispersive spectrometer. The composition of the rust layer was analyzed using an X-ray diffractometer and X-ray photoelectron spectrometer. The electrochemical properties of the chain steel were studied by measuring the open circuit potential, electrochemical impedance spectroscopy, and polarization curve.

## 2. MATERIALS AND METHODS

### 2.1. Material and hanging piece experiment

The main chemical composition of the chain steel, by mass, is as follows: 0.15% carbon (C), 0.40% silicon (Si), 0.70% manganese (Mn),  $\leq 0.025\%$  phosphorus (P),  $\leq 0.035\%$  sulfur (S), 0.95% chromium (Cr), 1.35% nickel (Ni), 0.20% molybdenum (Mo), and iron (Fe). Prior to the experiment, all samples were cleaned with 10% sodium hydroxide (NaOH) and 18% hydrochloric acid (HCl) to remove surface oil and rust. The sample size was  $(50 \pm 0.1) \text{ mm} \times (25 \pm 0.1) \text{ mm} \times (5 \pm 0.1) \text{ mm}$ . Three parallel samples were used in each group to calculate the weight loss rate. Samples measuring  $10 \text{ mm} \times 10 \text{ mm} \times 3 \text{ mm}$  were utilized for observing surface morphology, cross-section element distribution, and electrochemical measurements. The samples were polished

using SiC sandpaper with a mesh size of 1000–5000, followed by cleaning with deionized water and ethanol. A sample measuring 10 mm × 10 mm × 5 mm was used for the friction and wear experiment, and the surface wear morphology was observed. Additionally, the sample was treated and polished using the same method, apart from being weighed.

The detailed steps of the immersion and hanging plate experiment are as follows: 1. Weighing and recording the number with an accuracy of 0.01 g. 2. A mixed solution of six different chloride concentrations, consisting of desulfurization wastewater and slag water, was used. The chloride concentrations were 0.1%, 0.3%, 0.5%, 1%, 2%, and 3%, labeled as D0.1, D0.3, D0.5, D1, D2, and D3, respectively. Since the majority of the other ions in the solution are metal cations ( $\text{Ca}^{2+}$ ,  $\text{Mg}^{2+}$ ,  $\text{Na}^{2+}$ ) was significantly lower than that of chloride ions, it could be ignored. The pH was adjusted to 9, and the experiment was divided into three groups: pure corrosion, corrosive wear, and pure wear. The wear body used was the residue retrieved from the power plant. 3. To simulate the working environment of the slag extraction machine, the solution temperature was set to 60°C and the speed to 80rpm. The sample underwent reciprocating dry and wet cycles, with 60 seconds in the solution and 180 seconds in the air. 4. The sample was taken out and washed with clean water. Then, it was washed with 1000mL of hydrochloric acid (HCl,  $\rho = 1.19 \text{ g/mL}$ ), 20 g of antimony trioxide ( $\text{Sb}_2\text{O}_3$ ), and 50 g of stannous chloride ( $\text{SnCl}_2$ ) using an ultrasonic cleaner for 10 minutes. Afterward, it was dried in a dryer and weighed. Blank experiments were conducted for each group of experiments. 5. The sample was weighed, and the weight loss rate was calculated using the following formula:

$$v = (m_1 - m_2 - m_3) \times 8.76 \times 10^7 / stp \quad (1)$$

Where  $v$  is the corrosion rate, mm/y;  $m_1$  is the sample mass before the experiment, g;  $m_2$  is the sample mass after the experiment, g;  $m_3$  is the quality difference of blank sample before and after pickling, g;  $s$  is the total area of the sample, cm;  $t$  (120 h) is the test time, h;  $\rho$  ( $7.86 \times 10^3$ ) is the density of the material, kg/m<sup>3</sup>.

## 2.2. Experimental analysis of friction and wear

The friction and wear testing machine (HSR-2M type) was used to determine the friction coefficient. The results were measured in real-time using a computer, and the test results were output at specific intervals. The sample underwent reciprocation of 3 mm under a load of 10N and a motion speed of 5 HZ. After the movement, the wear mass was weighed and three groups of parallel samples were set in the experiment to ensure the accuracy of the results.

## 2.3. Characterization and measurement

After completing the experiment, the macro morphology of the sample was captured using a digital camera. The surface roughness was observed using an Olympus microscope after removing the corrosion products. The micromorphology and cross section morphology of the corrosion product films were examined using the JSM-6510A scanning electron microscope (SEM) manufactured by Nippon Electronics Co., LTD. Additionally, the element distribution of the corrosion product films was determined using the JED-2300 energy dispersive spectrometer (EDS).

The corrosion products on the sample's surface were analyzed using the Smartlab 9KW X-ray diffractometer (XRD) manufactured by Rigaku Co., LTD. The XRD was operated at a power of 4KW and a speed of 6°/min. The phase composition of the corrosion products was analyzed within the range of 10° to 90°.

The X-ray Photoelectron Spectrometer (XPS) manufactured by Thermo Fisher, a company based in the United States, was used to analyze the oxidation states of Fe, Cr, Ni, and Mo in the corrosion products after 5 days of corrosion. The XPS utilized X-ray radiation from Al K $\alpha$  ( $h\nu = 1486.6\text{eV}$ ) as the radiation source. The results obtained were carbon corrected.

## 2.4. Electrochemical measurement

The electrochemical measurements were conducted using a three-electrode system. The sample described in section 2.1. was connected to a copper wire and sealed with sealant on all surfaces except for a 1 cm<sup>2</sup> working area. This treated sample served as the working electrode, while a platinum electrode was used as the counter electrode and a saturated calomel electrode was used as the reference electrode. The bare leak sample and rust sample were tested in six different solutions, with the solution temperature maintained at 60°C in a water bath during the test. The open circuit potential of the bare samples was measured at 0.5 h, 1 h, 5 h, 12 h, and 24 h (hereafter referred to as T1, T2, T3, T4, T5) and monitored in real-time. The impedance value was measured

under the open circuit potential at different time intervals after the test to determine the initial corrosion resistance of the samples. To investigate the corrosion resistance of samples after the stabilization of the rust layer, samples were subjected to corrosion in desulfurization wastewater with varying chloride concentrations for 3, 4, and 5 days, followed by Electrochemical Impedance Spectroscopy (EIS) experiments. The EIS test frequency ranged from 0.01 Hz to 100,000 Hz, with an amplitude of 0.005. Prior to the experiment, a 30-minute open-circuit monitoring was conducted to ensure system stability.

Scanning electrochemical microscopes (SECM) utilize the principle of electrochemical work to measure the redox reactions of samples within the measurement range and output current signals in real time. The advantage of SECM lies in its ability to measure electrical signals on the surface of conductors, semiconductors, and insulators, with a measurement accuracy of up to ten nanometers. By analyzing the micro-area electrochemical signals obtained, the corrosion resistance of the sample can be characterized. The system used for the test is the Shanghai Chenhua CH1920D, which consists of three main components: the electrochemical system, the three-dimensional control system, and the computer monitoring system. The electrochemical system includes an electrolytic cell, a probe, and a double constant potential meter. The three-dimensional control system allows for precise control of the probe's movement over the sample at different speeds. The computer system is responsible for controlling the operating system, monitoring the electrical signals, and collecting and analyzing the data.

### 3. RESULTS AND DISCUSSION

#### 3.1. Weightlessness rate and surface morphology analysis

After the chain steel under investigation was cut and formed through the preparation and calibration process, the rust, oil, and other impurities on the surface were removed by shot blasting until the chain surface became bright. Subsequently, the chain was subjected to heat preservation at 930°C in a normalizing furnace for 8 hours, followed by air cooling. After that, carburization was carried out in a carburizing furnace at 920°C for 72 hours. The chain was then quenched and tempered at 180°C for 4 hours. This process resulted in obtaining tempered martensite with a black acicular microstructure, which exhibited high hardness and toughness [12], as shown in Figure 1.

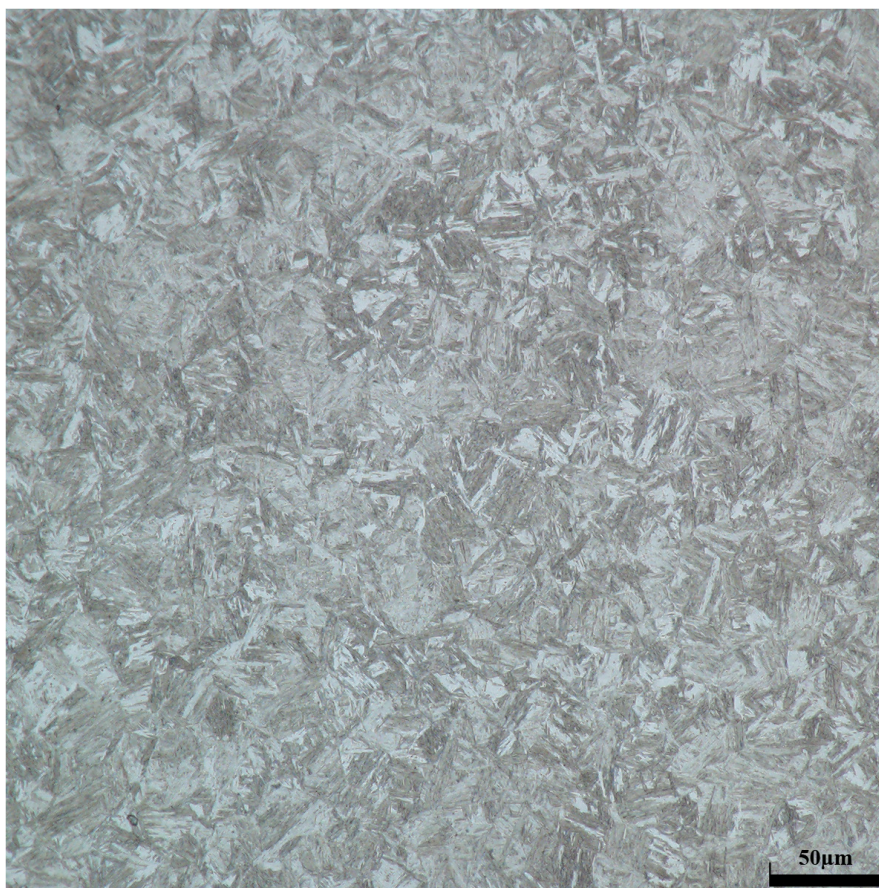


**Figure 1:** Metallographic structure of 17NiCrMo6 steel.

Figure 2 presents the weight loss rates of 17NiCrMo6 steel in desulfurization wastewater with different chloride concentrations, reflecting both corrosive wear and pure corrosion. The weight loss rate due to corrosive wear was found to be higher than that of pure corrosion, indicating that wear accelerates the corrosion process. As time progressed, the weight loss rate exhibited a decreasing trend, with decreasing amplitude, eventually reaching a relatively stable state after 3 days. This can be attributed to the gradual stabilization of the rust layer during the corrosion process, which provides protection to the underlying matrix. Furthermore,  $\text{Cl}^-$  acts in the early stage of corrosion, with the extension of time, as  $\text{Cl}^-$  promotes the thickening of the corrosion product film, the corrosion product film structure is more complete, and the content of incomplete oxidation product  $\text{Fe}_3\text{O}_4$  in the inner layer of the corrosion product film is increased, which leads to more difficult diffusion of  $\text{Cl}^-$  to the substrate, and a decrease in the rate of weight loss.  $\text{Cl}^-$  influences the characteristics and composition of the corrosion product film by directly or indirectly participating in the corrosion reaction [13]. After 5 days, sample D2 exhibited the lowest weight loss, while D0.3 displayed the highest weight loss. This suggests that the sample exhibits lower corrosion resistance at low chloride concentrations and higher corrosion resistance at high concentrations. Throughout the experiment, the weight loss rates at D0.1, D0.3, and D0.5 concentrations were significantly higher compared to D1, D2, and D3, thereby confirming the role of chloride ions in promoting the formation of corrosion products. It is noteworthy that the corrosion rate at different chloride concentrations exhibited two inflection points. When the chloride concentration is below D0.3, the rate of weight loss increases; when it exceeds D0.3, the rate decreases. However, when the chloride concentration surpasses D2, the weight loss rate begins to rise again, which may be attributed to the protective effect of the rust layer.

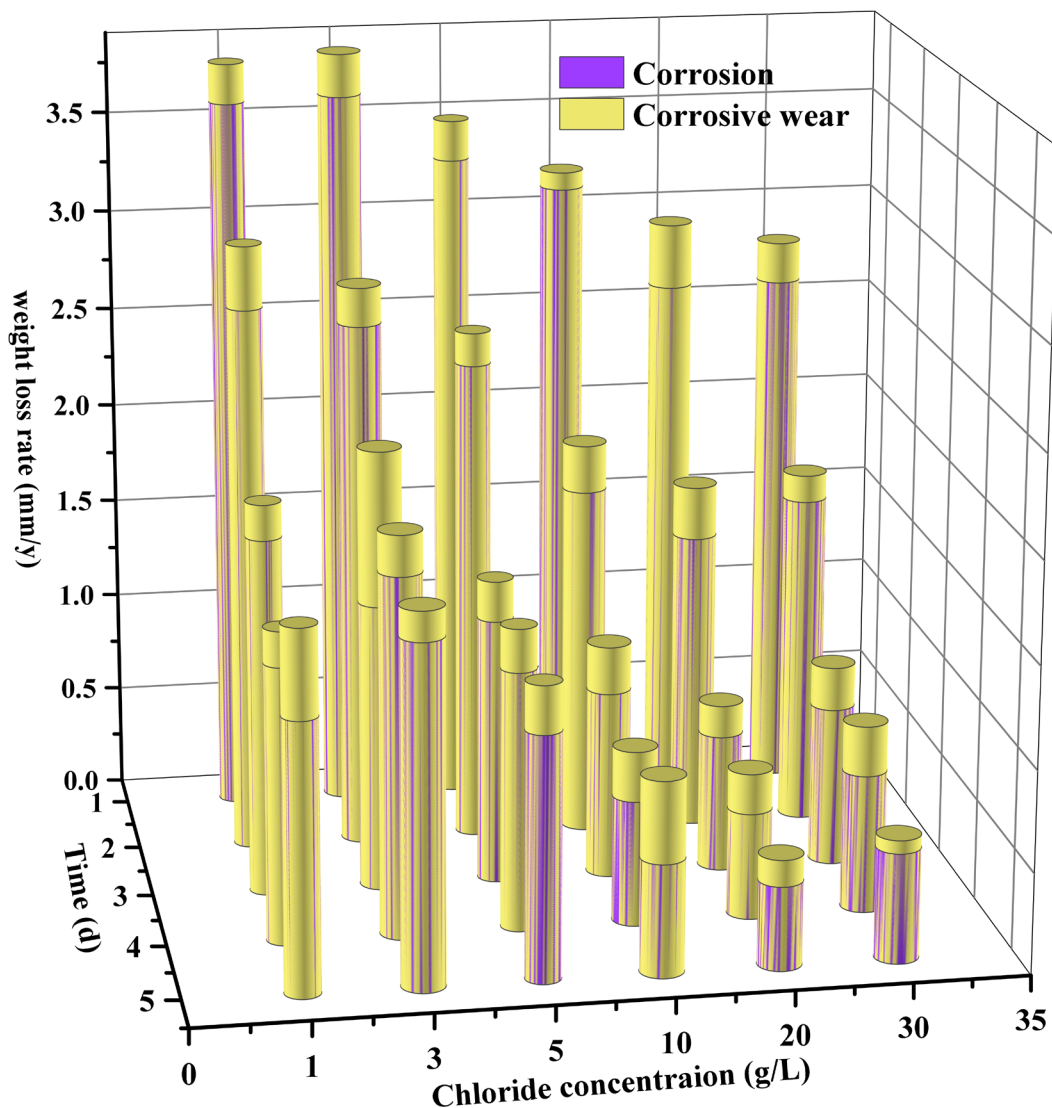


Figure 2: Weight loss rate of 17NiCrMo6 steel under 6 different concentrations of solution.

Previous studies [14–16] have indicated the presence of a critical concentration of chloride ions. Once the chloride ion concentration reaches a certain level, it causes a shift in the weight loss rate. D0.3 and D2 are clearly representative of this concentration. This phenomenon is largely dependent on the material's properties. The long-term corrosion rate of the sample is related to the type of rust formed during the initial stage of its exposure to the original surface, which will be explained further.

As illustrated in Figure 3, the surface of the samples in the interdip test, conducted in desulphurization wastewater with varying  $\text{Cl}^-$  concentrations, gradually changed from grayish black to reddish-brown and yellowish-brown. Different colors may indicate the formation of distinct corrosion products. The yellowish-brown rust primarily consists of oxidizing substances such as  $\text{Fe}_2\text{O}_3$ , while the reddish-brown rust mainly comprises oxidizing substances like  $\text{FeO}$  and  $\text{Fe}_3\text{O}_4$  [17–19]. It can be observed that with an increase in  $\text{Cl}^-$  concentration, the color of the rust deepens, suggesting a weakening of the oxidation degree and a reduction in the corrosion extent.

For the two samples exposed to low-concentration water samples, general corrosion was observed as the thickness of the rust layer and the corrosion area increased. When the chloride concentration reached D0.5, the uniform corrosion transformed into pitting corrosion, accompanied by a decrease in the coverage of corrosion products on the surface. This transition from uniform corrosion to pitting corrosion continues as the chloride concentration further increases.

However, the spread of local corrosion causes discrete pitting pits to converge, resulting in a phenomenon similar to general corrosion. This indicates that there is no strict boundary between different forms of corrosion in complex water quality environments [20]. In the case of corrosive wear, the mechanical loss caused by wear enlarges the corrosion pit. As a result, pitting is not observed at high concentrations, but the upwarped corrosion products can be seen. The mass loss caused by corrosive wear is significantly greater than that caused by pure corrosion. When compared to corrosive wear and pure wear, the corrosion caused by pure wear is minimal and can be considered negligible. Furthermore, as shown in Figure 4, its surface exhibits a network morphology without prominent wear marks.

To better study the microstructure of corrosion products, the corrosion product film on the sample was observed using SEM after 5 days of corrosion. This is shown in Figure 5. As the  $\text{Cl}^-$  concentration increases, the pores on the surface of the corrosion products gradually decrease. At low concentrations, the corrosion products

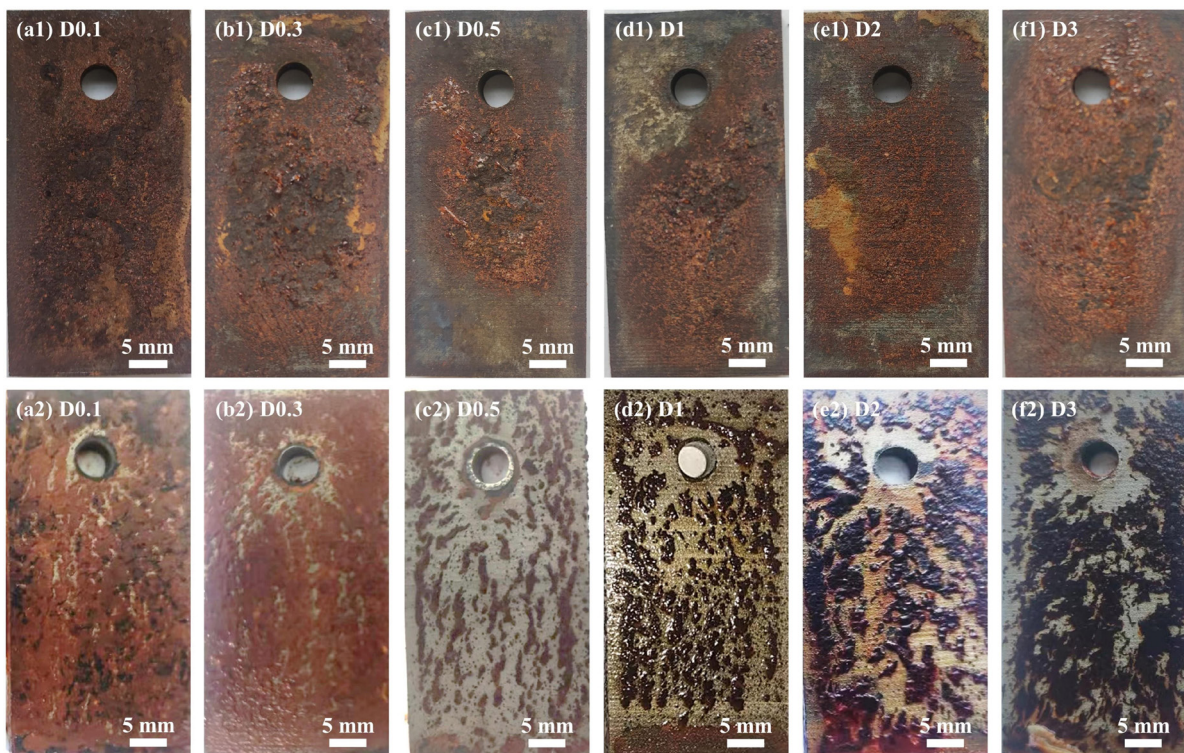


**Figure 3:** Corrosion wear morphology and corrosion morphology of 5d samples in desulphurization wastewater with different  $\text{Cl}^-$  concentrations: (a1), (b1), (c1), (d1), (e1), (f1), (a2), (b2), (c2), (d2), (e2), (f2).

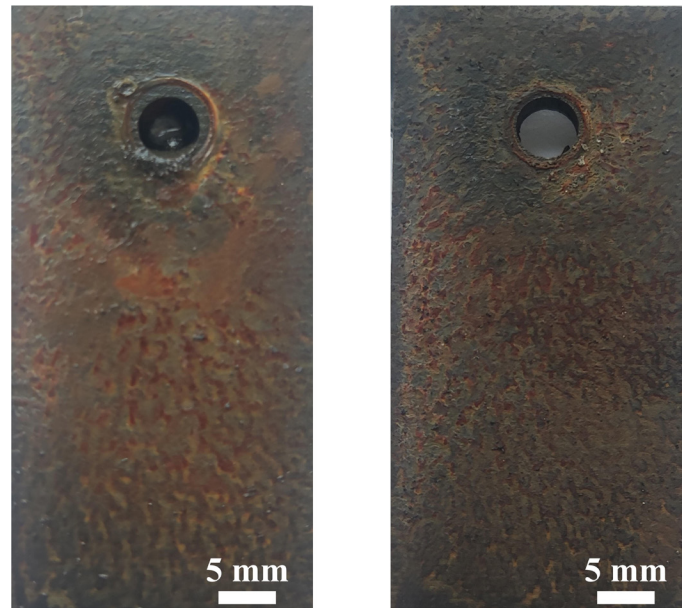


**Figure 4:** Surface morphology of distilled water after 5d of wear.

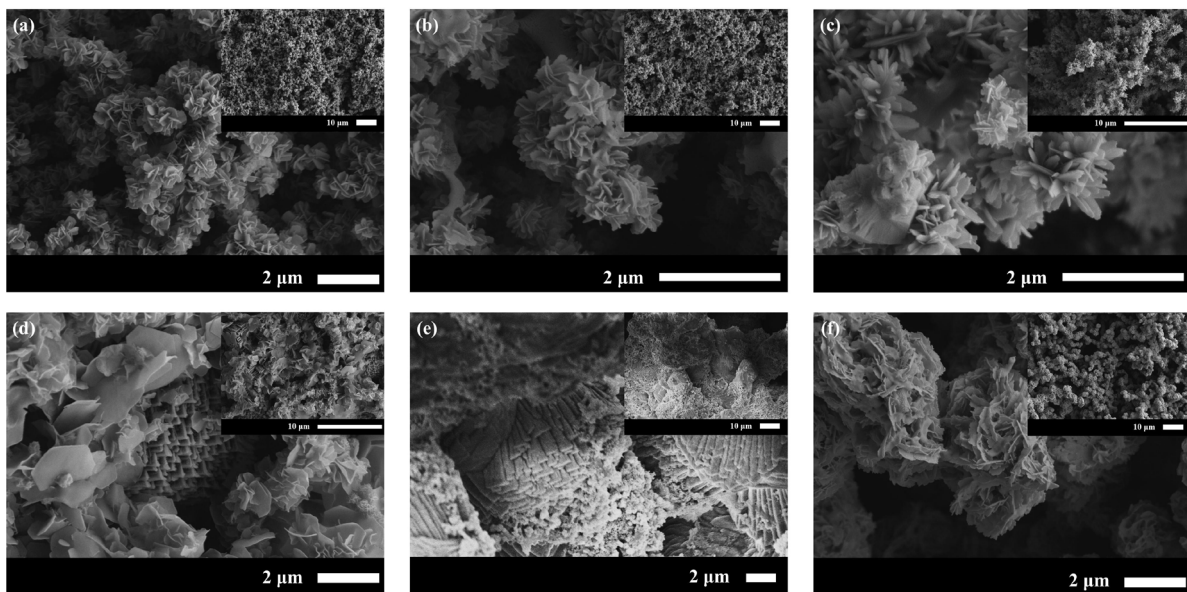


**Figure 5:** Micromorphology of corrosion products from desulfurization wastewater with different  $\text{Cl}^-$  concentrations: (a) D0.1, (b) D0.3, (c) D0.5, (d) D1, (e) D2, (f) D3.

consist of lamellar honeycomb structures (This structure is formed by the incomplete oxidation reaction of Fe as the environment changes from dry to wet during the dry-wet cycle to produce FeO), which then gather into cotton ball-like products, as shown in Figure 5a and 5b. This structure is obviously different from that of general hydroxide (Cotton balls or needles) and resembles FeO and other products. As the  $\text{Cl}^-$  concentration further increases, needle band products appear within the interleaved lamellar products, as shown in Figure 5c. This may indicate the formation of  $\gamma\text{-FeOOH}$  [21]. Figure 5d and 5e display mica-like and sand-like corrosion products. However, lepidocrocite crystals can also exhibit sand-like and flower-like structures, suggesting that the morphology of corrosion products is diverse and constantly changing with environmental variations [22]. As the concentration of the solution continued to increase, cotton-like globules started to form on the flower-like products at D3, possibly due to the transformation from  $\gamma\text{-FeOOH}$  to  $\alpha\text{-FeOOH}$  [23]. lepidocrocite ( $\alpha\text{-FeOOH}$ )

is known to be the most stable hydroxide of Fe, and under the right conditions, the transition to lepidocrocite ( $\alpha$ -FeOOH) is completed.

In summary, the corrosion product film becomes denser with increasing  $\text{Cl}^-$  concentration. It becomes looser again at D3. Different chlorine-containing desulphurization wastewater samples exhibit different microstructural characteristics in the rust layer. The presence of sandy and cotton ball-like features indicates the presence of gamma-FeOOH and  $\alpha$ -FeOOH, which are the main components of the rust layer [16]. Figure 5f illustrates the coexistence of these two corrosion products and their mutual transformation with changes in chloride content. The porous properties and discrete distribution of cotton ball-like products suggest the incomplete and non-uniform evolution of the corrosion product membrane structure. With the increase in chloride concentration (from D2 to D3), the dense corrosion layer transforms back into a porous and loose flower-like structure.

To further differentiate between pure corrosion, corrosive wear, and pure wear, the roughness of the cleaned sample was measured. Three points were selected on the sample surface to ensure data accuracy. Figure 6 depicts the 3D topography of the sample surface, while Table 1 presents the corresponding roughness values. As shown in Table 1, the roughness gradually decreases with increasing  $\text{Cl}^-$  concentration, reaching its lowest point at D2 (pure corrosion Ra 6.373  $\mu\text{m}$ , corrosion wear Ra 9.211  $\mu\text{m}$ ), and starts to rise again at D3 (pure corrosion Ra 8.142  $\mu\text{m}$ , corrosion wear Ra 11.563  $\mu\text{m}$ ). The sample surface transitions from flat to rough, indicating a shift from general corrosion to localized corrosion, gradually becoming a characteristic of general corrosion. Corrosion wear at low chloride concentrations (D0.1, D0.3) has a greater volume loss than the other two types of corrosion. Deeper corrosion pits were observed on the specimen surface. As shown in Table 1, the corrosive wear exhibits the highest roughness, followed by pure corrosion, while pure wear shows the lowest roughness. This observation is consistent with the aforementioned experimental results.

In general, the 17NiCrMo6 steel demonstrates excellent wear performance due to its high hardness and toughness. Under conditions of minimal corrosion, the wear degree is significantly reduced. Regarding roughness, Table 1 indicates a gradual decrease with increasing  $\text{Cl}^-$  concentration, reaching its lowest point at D2, followed by a subsequent increase at D3. The roughness of corrosive wear is the highest, followed by pure corrosion, and pure wear exhibits the least roughness. These findings align with the aforementioned experimental results. The mass loss caused by corrosion and wear alone and the mass loss caused by corrosive wear are not purely additive, where the interaction of corrosion and wear (corrosion accelerates wear and wear accelerates corrosion) also plays a key role in the mass loss, and in terms of roughness of the three different types of corrosion, corrosive wear is the roughest, with pure corrosion contributing much more to the roughness than pure wear. Overall, the 17NiCrMo6 steel exhibits minimal wear under conditions of almost no corrosion, thanks to its high hardness and toughness.

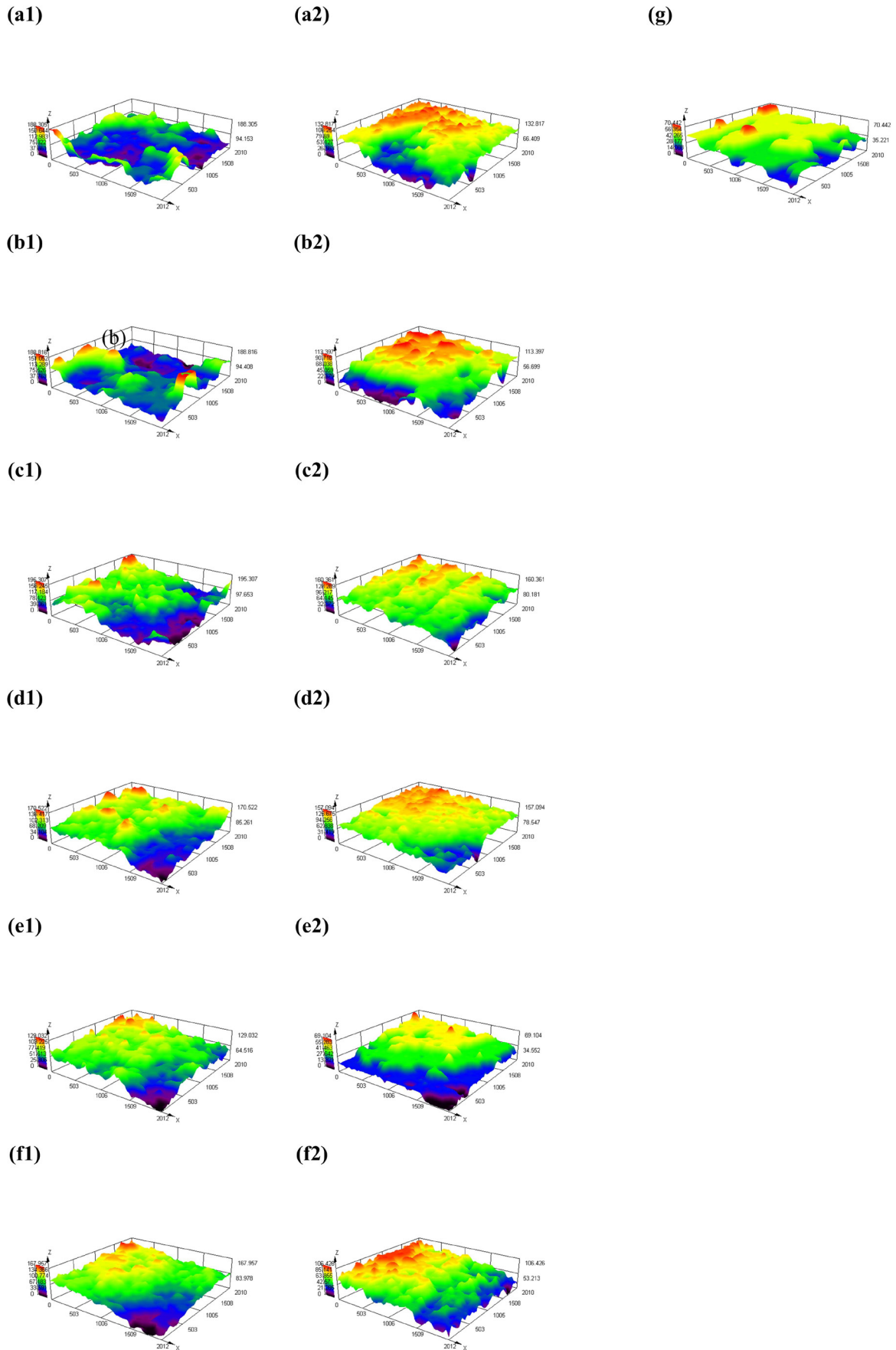
### 3.2. Friction and wear performance analysis

Figure 7 shows the wear morphology of 17NiCrMo6. At the initial stage of wear, there are noticeable scratches in the direction of wear, but no apparent cracks. However, as friction continues, these scratches widen due to fracture and shedding, resulting in some bumps, possibly caused by incomplete particle removal. In the final stage of wear, stepped scratches appear, increasing the contact area. This is also the main reason for the slight increase in the friction coefficient in this stage.

Figure 8 illustrates the experimental results of 17NiCrMo6 steel subjected to 1800 s of sliding dry friction treatment under a load of 10 N and a motion speed of 5 Hz. After multiple experiments, the average wear mass of the steel is determined to be 1.40mg. As depicted in Figure 8, the friction coefficient initially rises rapidly to approximately 0.55 and then continues to increase with fluctuations. From 400 to 1600s, the friction coefficient consistently remains between 0.6 and 0.7, occasionally dropping below 0.6 at certain points. In the final stage, the friction coefficient experiences a slight increase and stabilizes around 0.65. When other conditions remain constant, the magnitude of the friction coefficient is directly proportional to the actual contact area during the countergrinding process [24]. Although the polished specimen is not perfectly flat, its surface exhibits fine throw marks, which reduce the actual contact area. However, due to the significant difference in hardness between the two materials, these scratches will easily wear off, causing the friction coefficient to rapidly increase at the beginning. As friction progresses, the surface of the 17NiCrMo6 steel will deform or even break under pressure and cutting forces. The particles shed from the surface will then affect the real-time contact area, leading to sharp fluctuations in the friction coefficient.

In general, 17NiCrMo6 steel exhibits a low friction coefficient and relatively flat wear morphology, with no major scratches. This can be attributed to the high toughness and hardness of the tempered martensite formed after heat treatment. The tests conducted further confirm that corrosion plays a dominant role in the corrosive wear process, while the interaction between corrosion and wear has a secondary effect.





**Figure 6:** Pure corrosion 3D morphology, corrosion wear 3D morphology, and pure wear 3D morphology of D0.1~D3 samples after 5 d of mixed solutions: D0.1 (a1), D0.3 (b1), D0.5 (c1), D1 (d1), D2 (e1), and D3 (f1) corrosion wear 3D morphology, D0.1 (a2), D0.3 (b2), and D0.5 (c2), D1 (d2), D2 (e2), D3 (f2) corrosion profiles, (g) pure wear profiles.

**Table 1:** Three types of quality loss roughness.

	PURE CORROSION ( $\mu\text{m}$ )	CORROSIVE WEAR ( $\mu\text{m}$ )	PURE WEAR ( $\mu\text{m}$ )
D0.1	14.136	23.017	6.775
D0.3	13.829	21.987	
D0.5	11.290	17.355	
D1	10.014	14.377	
D2	6.373	9.211	
D3	8.142	11.563	

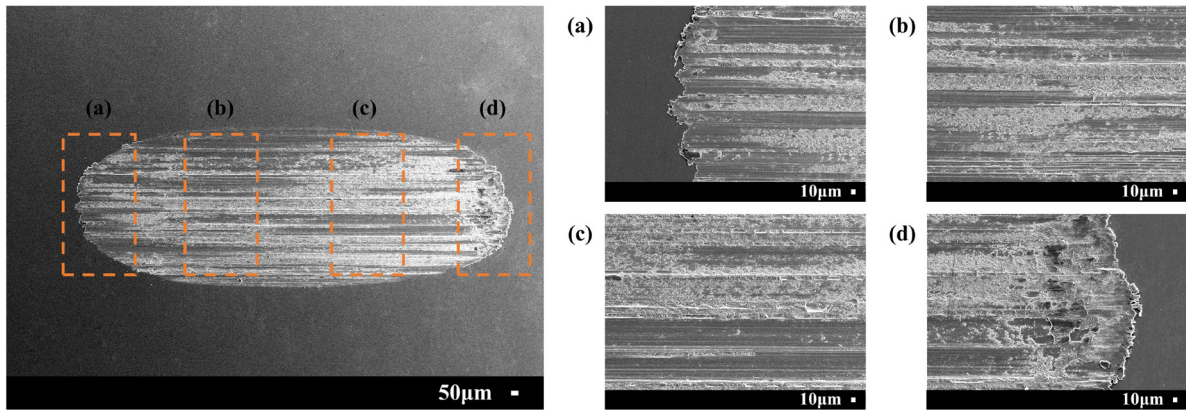


**Figure 7:** Wear morphology of 17NiCrMo6 steel.

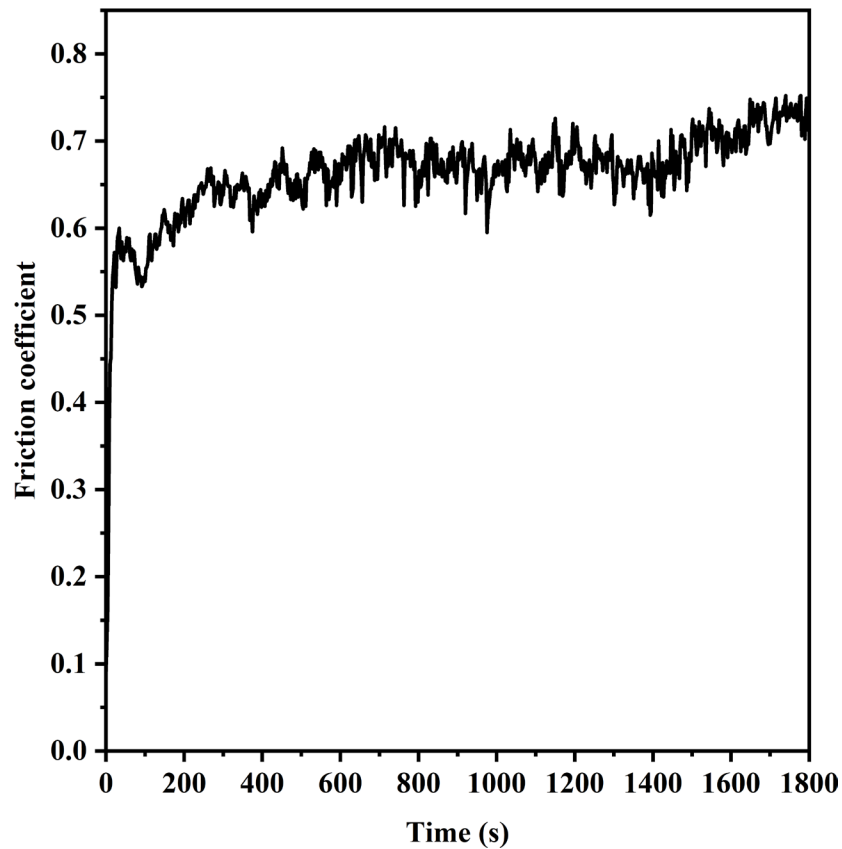


**Figure 8:** Friction coefficient curve of 17NiCrMo6 steel.

### 3.3. Section morphology and element distribution

Certain elements in carbon steel significantly affect the binding force between the rust layer and the matrix [25–27]. Therefore, analyzing the cross-section morphology of the rust layer, studying the distribution of elements, and investigating the role of corrosion resistance elements such as Cr, Ni, and Mo are essential for better understanding the corrosion mechanism of 17NiCrMo6 steel. As shown in Figure 9, the cross-section

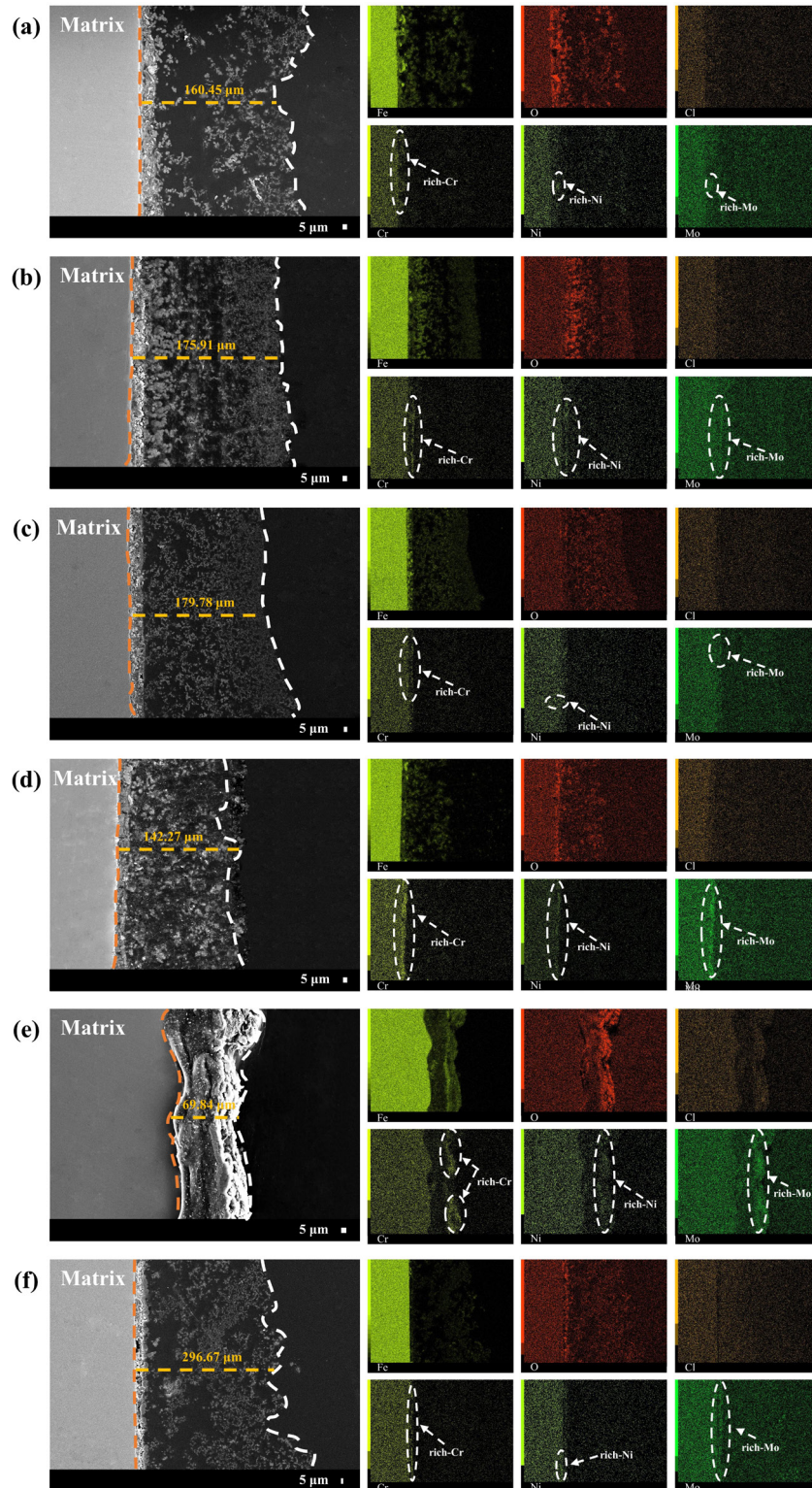


**Figure 9:** Cross section morphology and element distribution of the rust layer after 5 days of corrosion: (a) D0.1, (b) D0.3, (c) D0.5, (d) D1, (e) D2, (f) D3.

topography reveals that, apart from D2, the rust layer at other concentrations can be divided into an outer rust layer (ORL) and an inner rust layer (IRL). The outer rust layer exhibits a looser appearance with more holes compared to the inner rust layer. On the other hand, D2 only has a single layer of rust, which is dense and lacks cracks or holes. The thickness of the rust layer remains relatively consistent in four conditions, ranging from 140 to 180  $\mu\text{m}$ . Specifically, the thickness of D2 and D3 measures 69.84  $\mu\text{m}$  and 296.67  $\mu\text{m}$ , respectively. Based on the aforementioned analysis, it can be concluded that the density of the outer rust layer increases with the rise in chloride concentration. Once the outer rust layer reaches its peak and disappears, only the dense inner rust layer covers the surface of the matrix. This phenomenon can be attributed to the promotion of rust layer development towards a denser direction through the increase in  $\text{Cl}^-$  concentration.

To investigate the distribution of Fe, O, Cl, Cr, Ni, and Mo elements in the rust layer after 5 days of corrosion, EDS analysis was conducted. The resulting image, as shown in Figure 9, indicates the presence of element-rich areas, which were marked accordingly. It can be observed that Cr, Ni, Mo, and other elements converge in the inner rust layer, with the convergence area overlapping with O. This suggests the formation of a corrosion-resistant and dense oxide layer, in which these elements combine with O. Additionally,  $\text{Fe}_3\text{O}_4$  is attached to the substrate surface. At low concentrations, the enrichment is not prominent, with the rich area concentrated in a small region. However, as the concentration increases, the rich area gradually strengthens, displaying a brighter color and expanding towards the steel surface. This further confirms that an increase in concentration enhances the corrosion resistance of 17NiCrMo6 steel [28]. In addition to D2, element enrichment is observed in the inner rust layer and close to the matrix at all concentrations. On the other hand, D2 is located on the outer side of the entire rust layer, which explains the absence of an outer rust layer. This is due to the formation of a highly corrosion-resistant rust layer by D2, preventing  $\text{O}_2$  from penetrating and further reacting with the matrix. Therefore, it can be concluded that the concentration of  $\text{Cl}^-$  affects the role of alloying elements in the rust layer.

### 3.4. Composition analysis of rust layer

To understand the composition of the rust layer and the influence of  $\text{Cl}^-$  on it, the samples corroded for 5 days were analyzed using XRD, as shown in Figure 10. XRD analysis reveals the presence of  $\gamma\text{-FeOOH}$ ,  $\alpha\text{-FeOOH}$ ,  $\beta\text{-FeOOH}$ ,  $\gamma\text{-Fe}_2\text{O}_3$ ,  $\text{Fe}_3\text{O}_4$ , and some residual NaCl in the rust layer [29–31]. The peaks of  $\gamma\text{-Fe}_2\text{O}_3$ ,  $\text{Fe}_3\text{O}_4$ , and  $\gamma\text{-FeOOH}$  are similar, so they are grouped together.

♣  $\gamma\text{-FeOOH}$  ♥  $\beta\text{-FeOOH}$  ♦  $\alpha\text{-FeOOH}$  ●  $\text{Fe}_3\text{O}_4$  ♠  $\gamma\text{-Fe}_2\text{O}_3$  \* NaCl

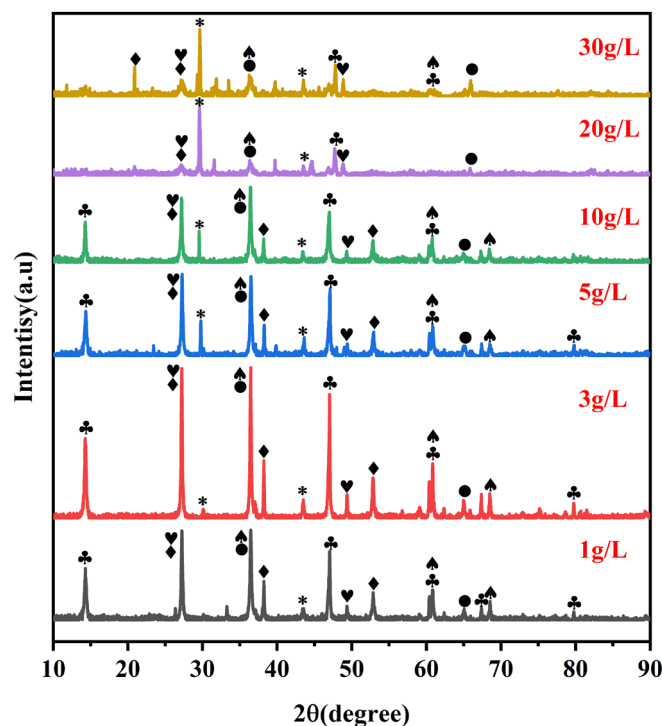


**Figure 10:** Phase composition of corrosion products of 17NiCrMo6 steel after 5 days of corrosion.

These corrosion products are commonly found in hot and humid environments. As the concentration increases, the NaCl content in the rust layer also increases, leading to higher peak intensity of NaCl. The peak intensity of  $\gamma$ -FeOOH at  $2\theta = 15^\circ$  gradually decreases with increasing chloride concentration, and becomes almost invisible at D2. Generally,  $\beta$ -FeOOH also increases with increasing chloride concentration [31]. A high chloride concentration promotes the deposition of  $\beta$ -FeOOH, which makes the corrosion layer more porous and accelerates the corrosion process. However, this phenomenon was not observed in 17NiCrMo6 steel with increasing chloride concentration.

To better understand the role and forms of Fe, Ni, Cr, and Mo elements in the inner rust layer, XPS tests were conducted on the samples after 5 days of corrosion. For detailed analysis, refer to Figures 11, 12, 13, and 14. The results show that the corrosion products are similar across the six different concentrations of solutions [29, 30, 32–34]. Fe is found in two forms,  $\text{Fe}_3\text{O}_4$  and FeOOH, and is combined with  $\text{Fe}_2\text{O}_3$  under D0.3, D0.5, and D1. Two forms of Ni,  $\text{NiFe}_2\text{O}_4$  and  $\text{Ni}(\text{OH})_2$ , are present.  $\text{Ni}(\text{OH})_{2\text{sat}}$  is the associated peak of  $\text{Ni}(\text{OH})_2$ , while NiO is formed under D0.3 and D1. NiO is formed by dehydrating  $\text{Ni}(\text{OH})_2$ , and both  $\text{Ni}(\text{OH})_2$  and NiO react with  $\text{Fe}(\text{OH})_2$  to form  $\text{NiFe}_2\text{O}_4$ . Molybdenum (Mo) also presents two forms:  $\text{Mo}^{4+}$  and  $\text{Mo}^{6+}$ . Table 2 shows the semi-quantitative results of XPS analysis on the role of matter in the inner rust layer for quantitative analysis of these compounds. From Table 2, it can be observed that the  $\text{Fe}_3\text{O}_4$  content is the lowest in D0.3 and the highest in D2. Since  $\text{Fe}_3\text{O}_4$  is the main component of the inner rust layer, its content directly affects the quality of the rust layer. As the  $\text{Cl}^-$  content increases, its inhibitory effect on the growth of the inner rust layer transitions into a promotion effect. Once the critical value is reached,  $\text{Cl}^-$  penetrates the rust layer, causing a decline in the protective effect of the rust layer. The ratio of  $\text{Cr}(\text{OH})_3$  to  $\text{Cr}_2\text{O}_3$ , the two combined forms of chromium (Cr), is close to 3:2 at lower and higher concentrations, while it becomes 1:1 at medium concentration.  $\text{NiFe}_2\text{O}_4$  contributes positively to the densification of the rust layer, with the lowest content in D0.3 and the highest content in D2. With an increase in  $\text{Cl}^-$  concentration, the steel matrix is more inclined to produce  $\text{Mo}^{6+}$ , and the content of  $\text{Mo}^{6+}$  is significantly higher than that of  $\text{Mo}^{4+}$ , indicating the greater stability of  $\text{Mo}^{6+}$ .

### 3.5. Electrochemical performance analysis

The corrosion rate is primarily determined by the type of corrosion that the matrix forms at the initial stage of corrosion [20]. While much research has been conducted on the influence of long-term corrosion, there is a

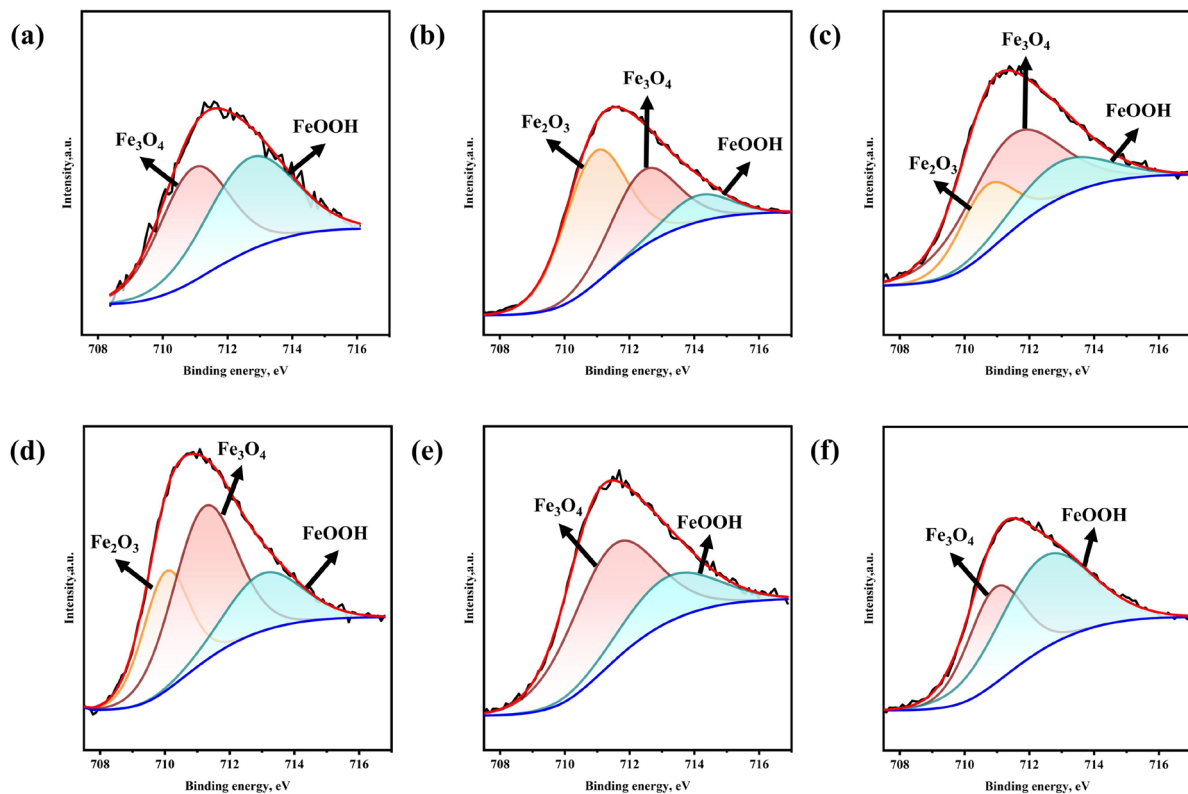


**Figure 11:**  $\text{Fe}_{2p_{3/2}}$  spectra of 17NiCrMo6 steel after corrosion in D0.1~D3 solution for 5 days.

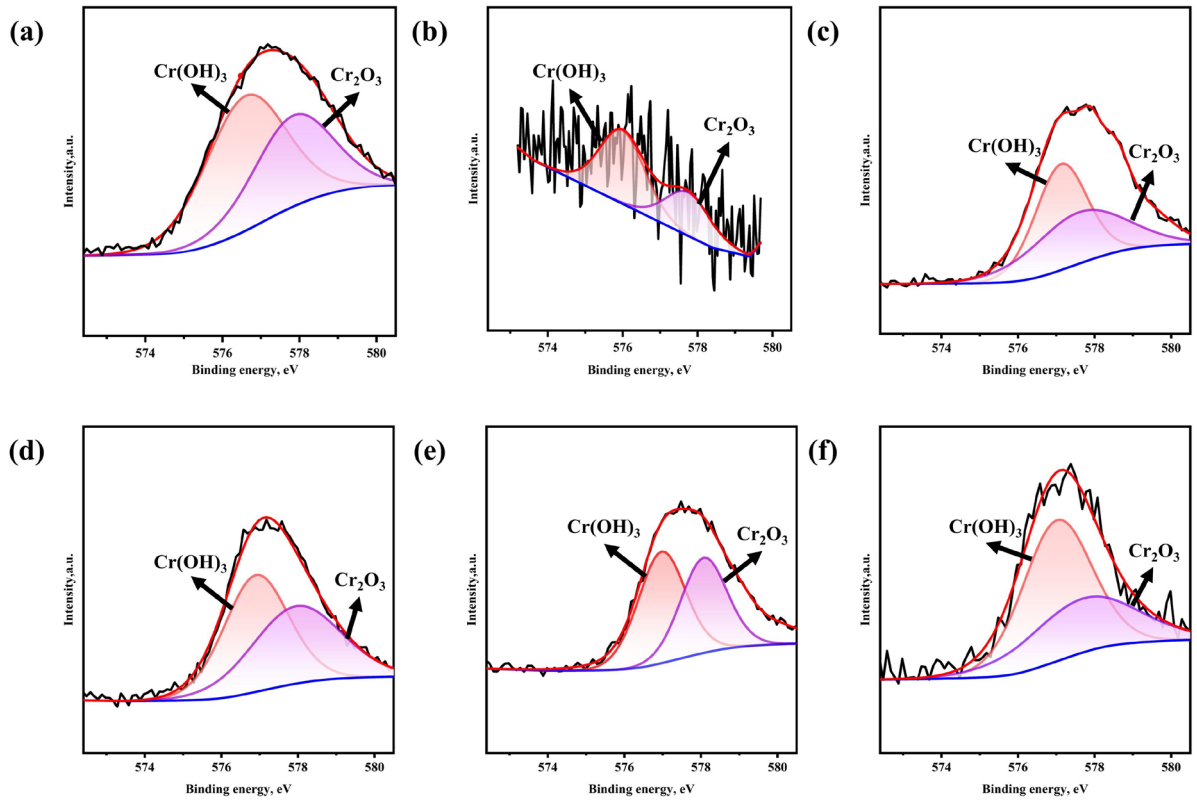


Figure 12: Cr<sub>2p<sub>3/2</sub></sub> spectrum of 17NiCrMo6 steel corroded in D0.1~D3 solution for 5 days.

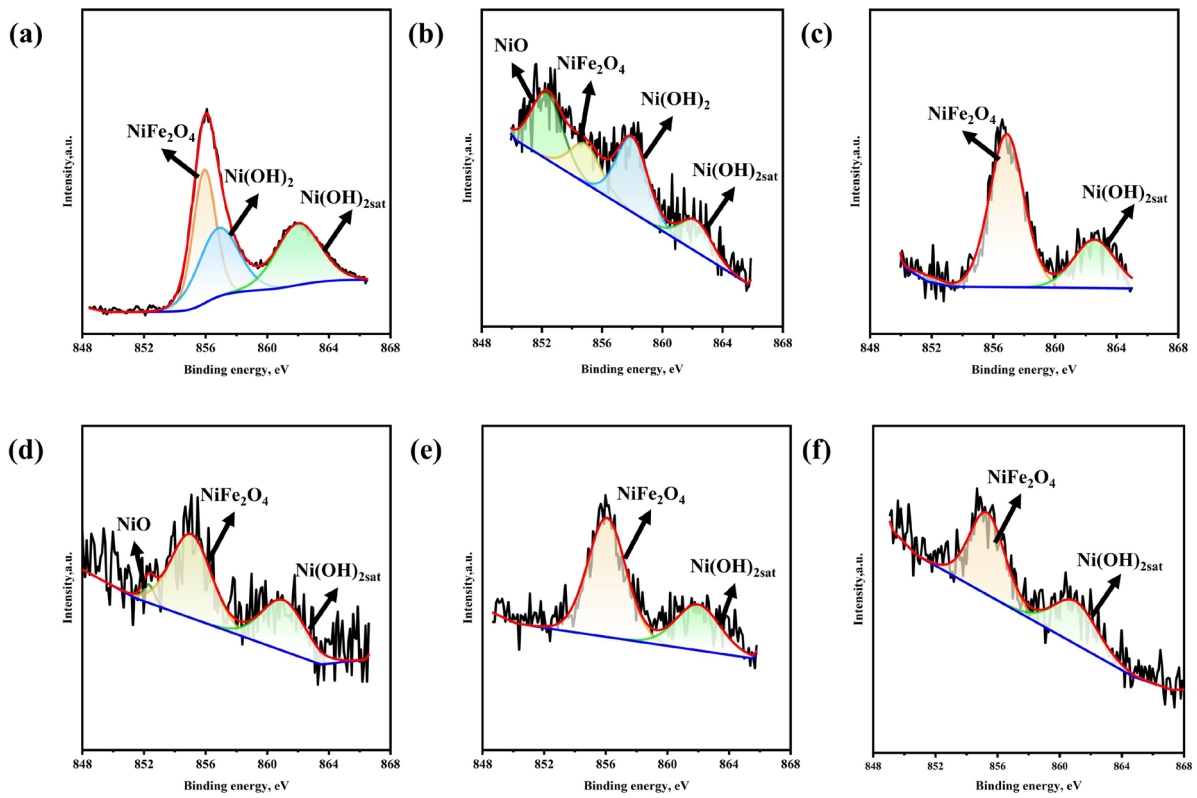
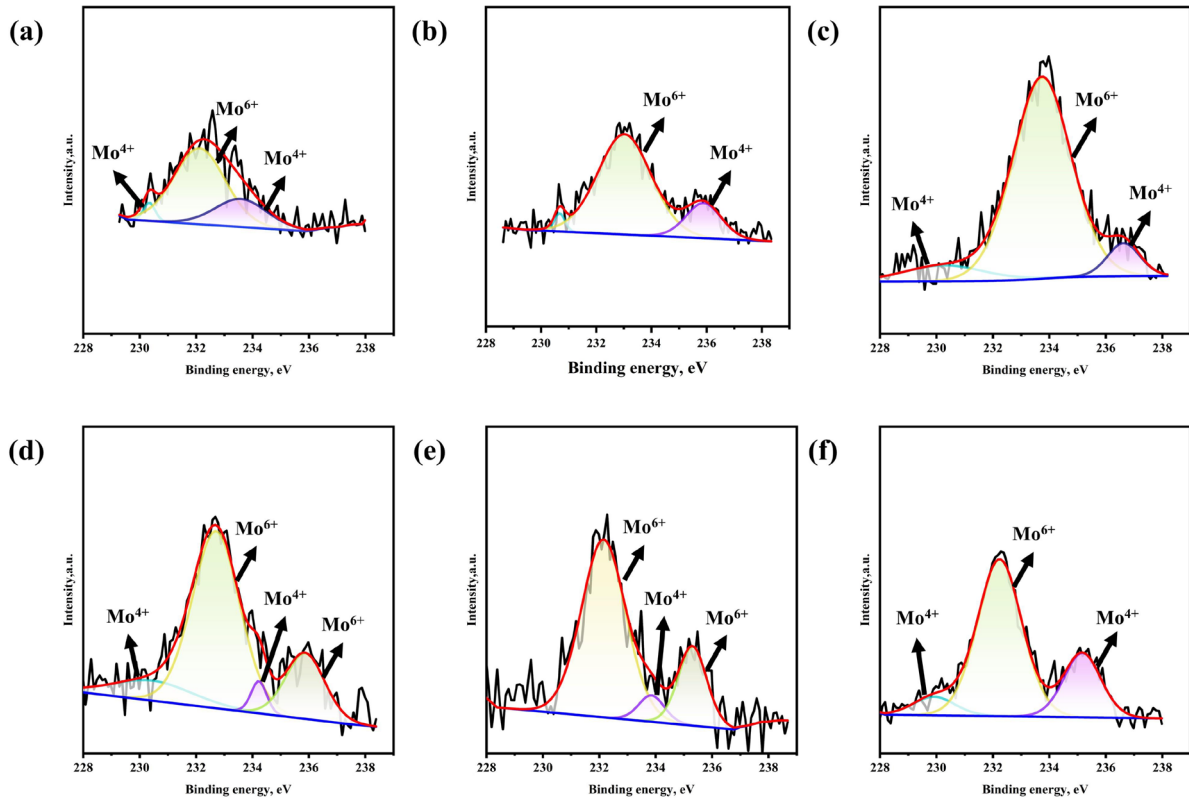


Figure 13: Ni<sub>2p<sub>3/2</sub></sub> spectrum of 17NiCrMo6 steel corroded in D0.1~D3 solution for 5 days.



**Figure 14:** Mo<sub>3d5/2</sub> spectrum of 17NiCrMo6 steel corroded in D0.1~D3 solution for 5 days.

**Table 2:** Content ratio of each phase element in the inner rust layer after 5d corrosion.

ELEMENTS	CHEMICAL STATES	PERCENTAGE OF EACH CHEMICAL STATE IN DIFFERENT SOLUTIONS (%)					
		D0.1	D0.3	D0.5	D1	D2	D3
Fe	Fe <sub>2</sub> O <sub>3</sub>	49.17	55.31	23.16	27.77	66.49	61.56
	Fe <sub>3</sub> O <sub>4</sub>	50.83	33.39	55.69	49.88	33.51	38.44
	FeOOH		11.31	21.15	22.35		
Cr	Cr(OH) <sub>3</sub>	61.95	62.90	53.55	52.17	54.40	62.18
	Cr <sub>2</sub> O <sub>3</sub>	38.05	37.10	46.45	47.83	45.60	37.82
Ni	NiO	35.31	31.11	69.05	3.56	70.52	60.35
	NiFe <sub>2</sub> O <sub>4</sub>	64.69	18.54	29.48	38.41	30.95	39.65
	Ni(OH) <sub>2</sub>		50.35		58.03		
Mo	Mo <sup>4+</sup>	32.01	18.40	9.11	16.10	6.32	7.63
	Mo <sup>6+</sup>	67.99	81.60	90.89	83.9	93.68	92.37

lack of discussion and analysis regarding the initial corrosion process. In order to further investigate the initial corrosion behavior of 17NiCrMo6 steel in desulphurization wastewater with varying chloride concentrations, a 24-hour open circuit potential detection was conducted on the bare steel sample, as displayed in Figure 15.

It is evident that the self-corrosion potential decreases rapidly within 1.39 hours (5000 seconds), levels off, and tends to stabilize at 5 hours (18000 seconds). This suggests that the change in chloride concentration does not affect the trend of change, and all of them reach a stable period at a similar time. A lower  $E_{\text{corr}}$  value indicates a higher risk of corrosion [35]. From the figure, it can be observed that D2 and D3 concentrations have the highest self-corrosion potential and are the most resistant to corrosion, followed by D1 and D0.5. D0.1 and D0.3 have the lowest potential. This aligns with the previous experimental results, indicating that after the initial corrosion type is formed, 17NiCrMo6 steel is more prone to corrode in a low concentration chloride solution and has the highest risk of corrosion at D0.3 concentration.

To gain a better understanding of the electrochemical properties of 17NiCrMo6 steel, polarization curves were generated after a 30-minute open circuit potential (OCP) test, as shown in Figure 16. The corrosion potential ( $E_{\text{corr}}$ ) and current density ( $I_{\text{corr}}$ ) after fitting are presented in Table 3. From the figure, it can be observed that the self-corrosion potentials of the curves are generally similar, except for D0.3, which has the highest

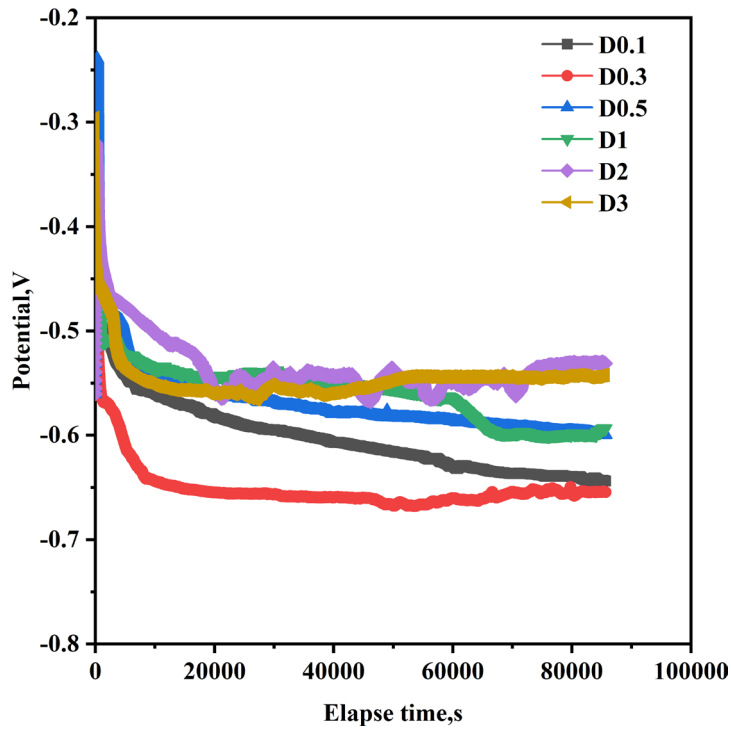


Figure 15: OCP evolution of 17NiCrMo6 steel at 6 concentrations.

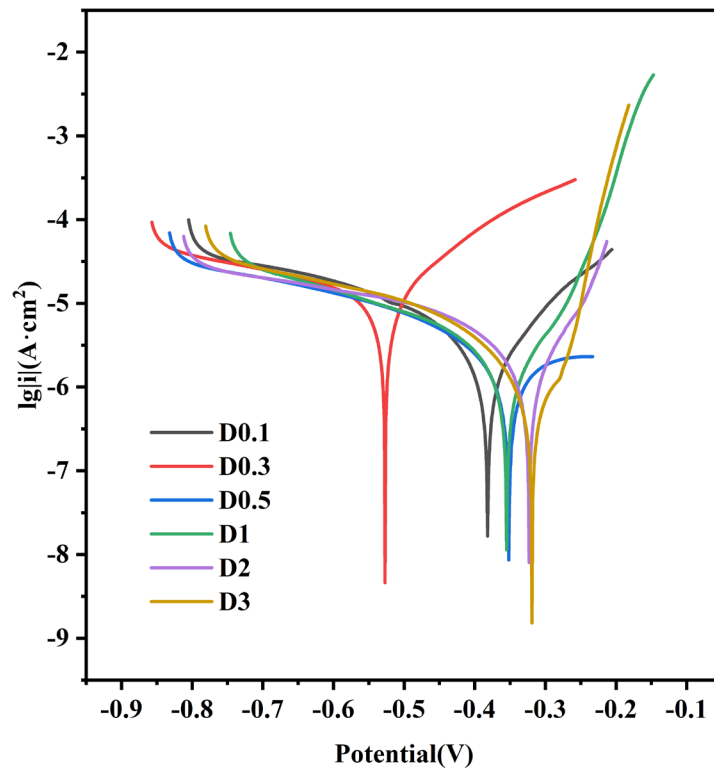


Figure 16: Polarization curve of 17NiCrMo6 steel.



**Table 3:** Polarization data for 17NiCrMo6 steel.

LABEL	$I_{Corr}$ (A/cm <sup>2</sup> )	$E_{Corr}$ (V)
D0.1	$2.2340 \times 10^{-6}$	-0.3826
D0.3	$1.6490 \times 10^{-5}$	-0.5286
D0.5	$3.6530 \times 10^{-6}$	-0.3524
D1	$1.2160 \times 10^{-6}$	-0.3551
D2	$1.1740 \times 10^{-6}$	-0.3244
D3	$1.7180 \times 10^{-6}$	-0.3177

self-corrosion current density. On the other hand, D2 exhibits the lowest self-corrosion current density. Since the self-corrosion current density and corrosion rate are directly proportional, it can be concluded that D0.3 has the highest corrosion rate, while D2 has the lowest. This conclusion aligns with the results of the weightlessness experiment. This indicates that as the concentration of Cl<sup>-</sup> increases, its invasion into the sample matrix also increases, accelerating the corrosion rate. However, with a further increase in Cl<sup>-</sup> concentration, the generation of a corrosion product film on the surface of the steel is promoted, leading to a decrease in the corrosion rate until it reaches a critical value. At this point, Cl<sup>-</sup> once again penetrates the corrosion product film, causing the corrosion rate to rise again.

To further investigate the interfacial evolution process and electrochemical behavior of 17NiCrMo6 steel, an EIS test was conducted after monitoring the open circuit potential, as depicted in Figure 17 and Figure 18. The fitting data can be found in Table 4. Among them,  $R_s$ ,  $R_p$ , and  $R_{ct}$  represent solution resistance, corrosion product resistance, and charge transfer resistance, respectively. The impedance value of CPE can be calculated using the following formula [35, 36]:

$$Z = Y_0^{-1} \times (j\omega)^{-n} \quad (2)$$

$Y_0$  ( $\Omega^{-1} \times \text{cm}^{-2} \times \text{s}^{-n}$ ) is related to the modulus of the CPE, and  $n$  is a constant of 0–1. It can be observed that all Nyquist curves consist mainly of capacitive arcs. Additionally, the Nyquist curves at all times of D0.1–D0.5 exhibit a certain degree of low-frequency induced contraction, which is only found at 0.5h and 1h on D1 and D2, with no low-frequency induced contraction observed in D3. This low-frequency induced shrinkage is an inductive behavior that may be due to inhomogeneous adsorption of corrosion product ions [36]. However, this phenomenon gradually disappears with the increase in chloride concentration and the passage of time, indicating that chloride concentration affects the adsorption of corrosion product ions to some extent. The impedance arc shown in the figure is not a perfect semicircle, which suggests that the rust layer is heterogeneous (non-uniform and non-monotonic) [37–39], consistent with the above results. In terms of the size of the impedance arc, the impedance arc of D0.1 and D0.3 at 24h is smaller than that at 0.5h, the impedance arc of D0.5 gradually increases with time, the impedance arc of 24h slightly decreases on D1, and the impedance arcs of D2 and D3 are significantly larger than those of other concentrations. It can be seen from Table 4 that the corrosion in D2 exhibits the highest  $R_p$  after 5d.  $CPE_1$  and  $R_p$  represent the behavior of the corrosion product film. A higher  $R_p$  indicates a higher quality of the rust layer and better corrosion resistance. Under the conditions of D0.1, D0.3, and D0.5, there is no significant difference in the initial stage of the capacitive arc. However, compared to high concentration, low concentration exhibits higher corrosion stability. These phenomena indicate the complexity of the corrosion process, as the role of the corrosion product film in the initial stage is yet to be determined. The formation of the rust layer does not always have a positive effect on the protection of the matrix and can sometimes accelerate the corrosion reaction. By promoting the continuous thickening and compaction of the rust layer, high chloride concentration limits the diffusion of oxygen and the cathode reaction, thereby inhibiting the corrosion process. This further demonstrates the multiple effects of Cl<sup>-</sup> on the corrosion kinetics of carbon steel, as it can both accelerate corrosion and promote the growth of the corrosion layer, achieving the desired effect of inhibiting the corrosion reaction. The EIS data was fitted using ZSimpWin 2.0 software, and the fitting circuit is illustrated in Figure 19.

To compare the electrochemical properties of the samples with rust layer over time and concentration, EIS tests were conducted on 17NiCrMo6 steel after corrosion for 3d, 4d, and 5d under 6 different conditions. The results were presented in Figure 20, and the fitting results are shown in Table 5. With the increase in time, the radius of the impedance arc decreases under all conditions, indicating that the initially formed rust layer becomes loose due to the intrusion of Cl<sup>-</sup> and the protective effect deteriorates [40]. Additionally, D2 consistently exhibits

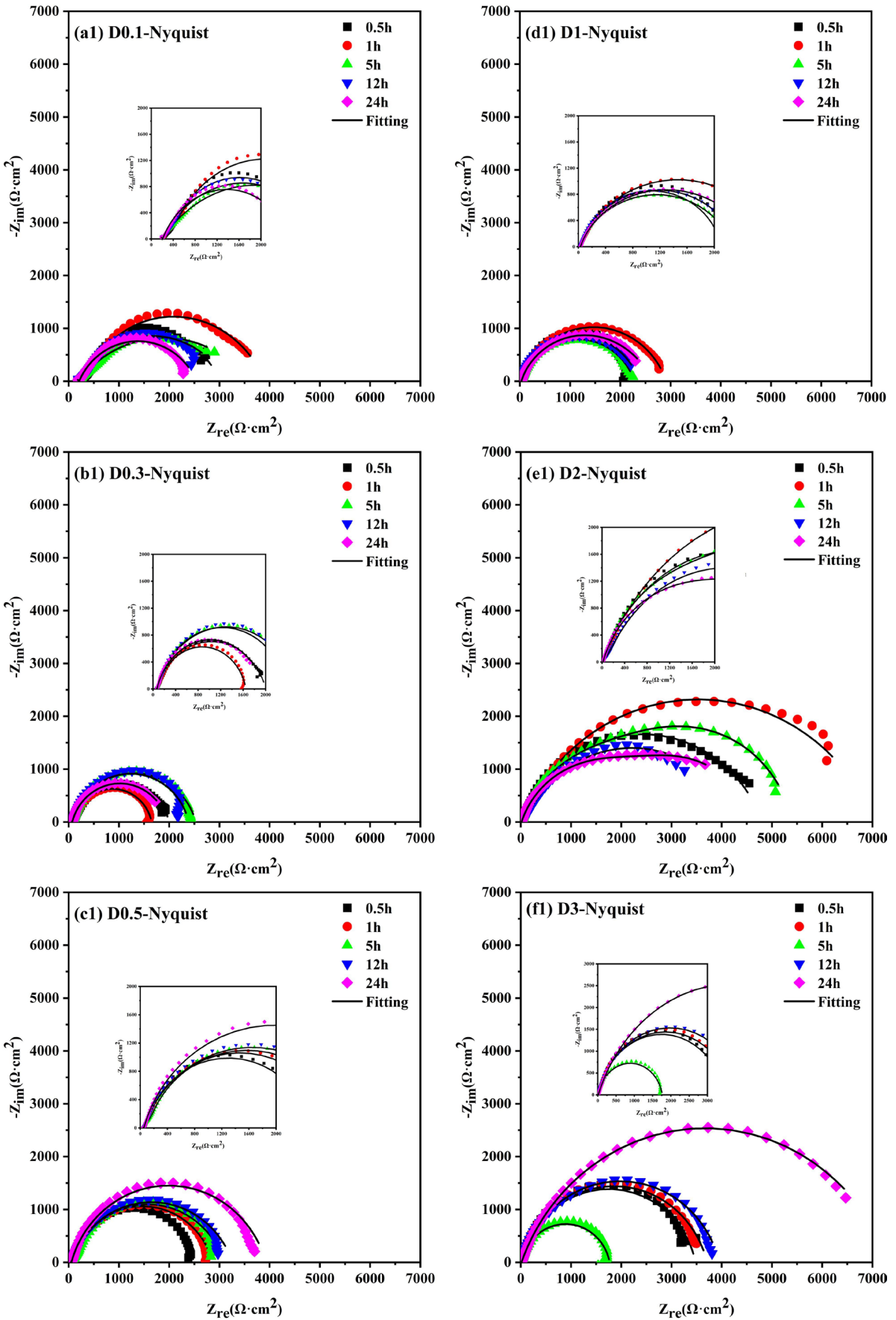
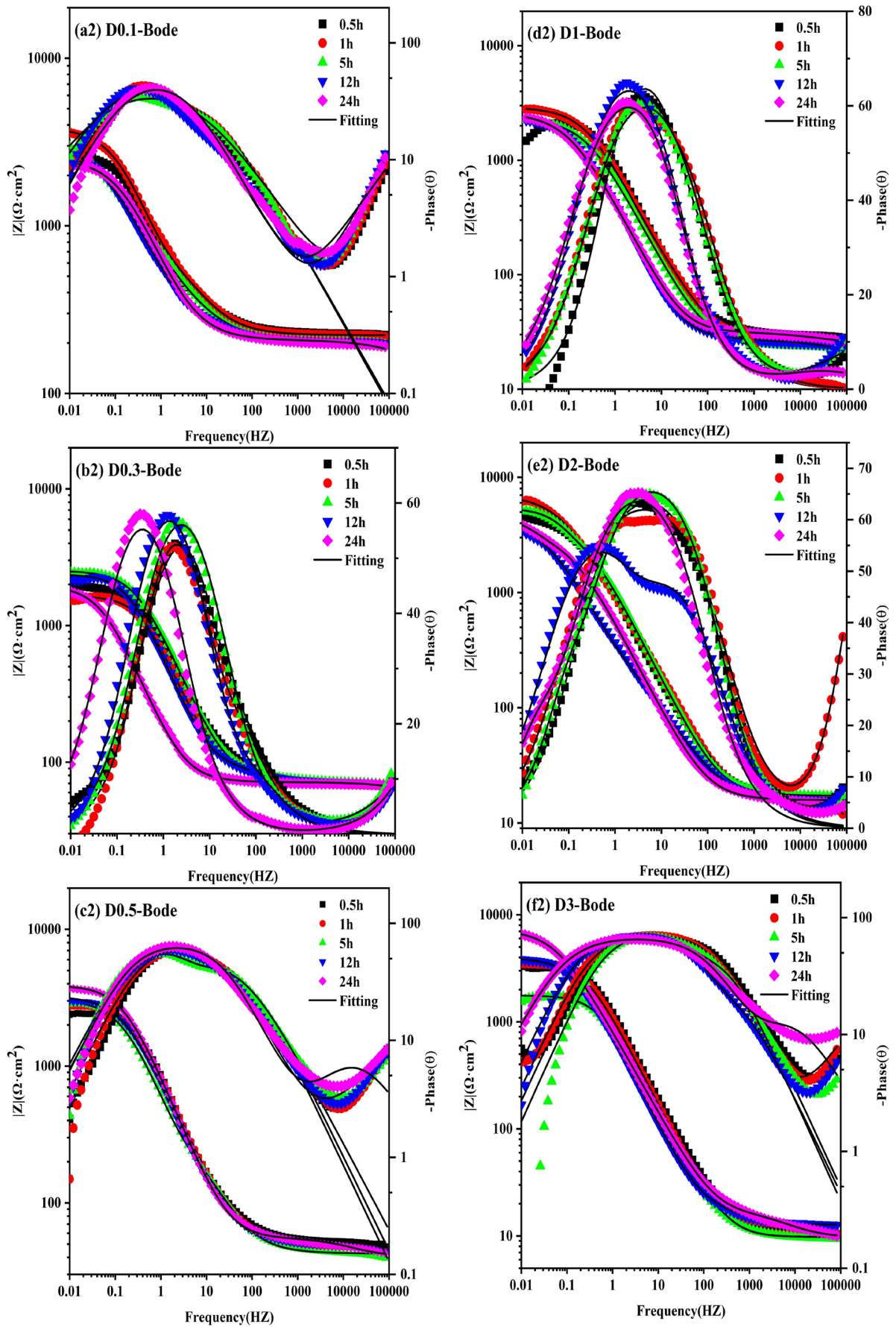


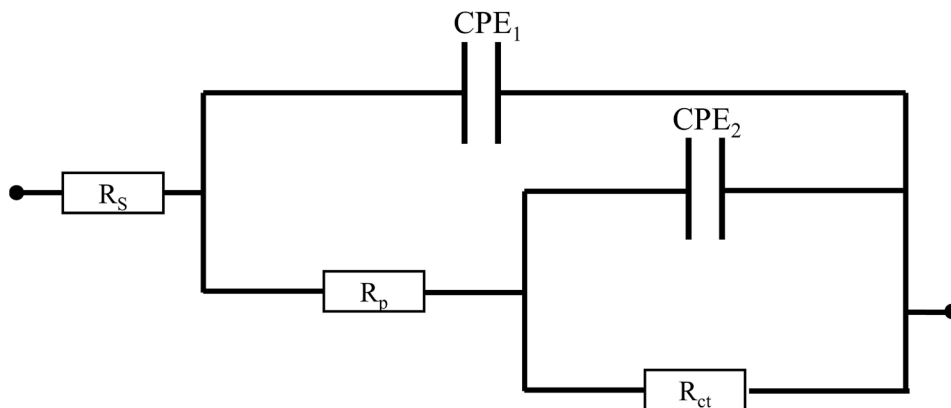
Figure 17: 17NiCrMo6 steel Nyquist after 24 h open-circuit monitoring: (a1) 1 g/L, (b1) 3 g/L, (c1) 5 g/L, (d1) 10 g/L, (e1) 20 g/L, (f1) 30 g/L.



**Figure 18:** 17NiCrMo6 steel Bode after 24 h open-circuit monitoring: (a2) 1 g/L, (b2) 3 g/L, (c2) 5 g/L, (d2) 10 g/L, (e2) 20 g/L, (f2) 30 g/L.

**Table 4:** Electrochemical parameters after corrosion product film fitting.

SOLUTION (g/L)	TIME (d)	$R_s$ ( $\Omega \text{ cm}^2$ )	$CPE_1 10^{-4}$ ( $\Omega^{-1} \text{ cm}^{-2} \text{ S}^{-n}$ )	$n_1$	$R_p$ ( $\Omega \text{ cm}^2$ )	$CPE_2 10^{-4}$ ( $\Omega^{-1} \text{ cm}^{-2} \text{ S}^{-n}$ )	$n_2$	$R_{ct}$ ( $\Omega \text{ cm}^2$ )
1	T1	227.1	2.719	0.6873	418.2	1.662	0.9487	2370
	T2	222.5	2.547	0.6999	811.5	1.700	0.9181	2875
	T3	189.4	1.809	1.0000	198.5	5.797	0.5738	3396
	T4	233.5	1.799	0.7423	211.4	6.364	0.6741	2920
	T5	210.1	1.339	0.6016	208.2	4.594	0.7325	2337
3	T1	68.98	2.092	0.7659	147.7	0.7737	0.9136	1790
	T2	69.10	1.546	0.8425	99.00	1.653	0.8827	1484
	T3	69.31	1.633	0.5791	75.04	2.512	0.8226	2456
	T4	70.63	1.463	0.8435	42.89	2.216	0.8620	2274
	T5	67.62	1.379	0.7164	71.33	14.26	0.8438	1896
5	T1	52.09	1.3350	0.8317	136.8	0.8743	0.9164	2336
	T2	47.24	1.5740	0.8107	120.1	0.8836	0.8489	2704
	T3	42.65	2.660	0.7452	431.0	1.282	0.9512	2635
	T4	41.25	0.8001	0.7287	56.32	1.832	0.8599	3215
	T5	40.27	0.2238	0.7104	15.37	2.379	0.8291	3875
10	T1	29.82	1.0370	0.8791	81.93	0.7962	0.8878	1990
	T2	26.28	2.4490	0.7768	105.6	0.2498	1.000	1830
	T3	28.34	0.1214	0.6727	24.51	3.117	0.7824	2256
	T4	26.07	0.4705	0.4076	27.84	4.832	0.8397	2381
	T5	23.93	1.6630	0.5551	7.942	4.193	0.8315	2623
20	T1	17.23	1.8390	0.8132	16.75	2.456	0.7719	4794
	T2	16.89	1.0480	0.9905	14.78	2.632	0.7419	7038
	T3	17.22	2.0260	0.8049	3919	12.49	0.9785	1487
	T4	15.58	4.9990	0.7712	376.1	3.460	0.7796	3977
	T5	15.78	4.1540	0.7884	3206	57.96	0.9369	1337
30	T1	10.68	1.250	0.8496	159.1	0.2929	0.9010	3313
	T2	9.781	3.948	0.6264	11.53	1.765	0.8475	3699
	T3	9.778	1.355	0.8714	50.92	0.7769	0.8963	1708
	T4	12.76	1.669	0.8277	16.08	1.138	0.8729	3926
	T5	9.627	0.7653	0.7213	8.145	2.148	0.7906	7320

**Figure 19:** Fitting circuit for EIS test.

the largest impedance arc and a diffusion tail, suggesting a more challenging diffusion process. The improved performance can be attributed to the continuous thickening and compaction of the rust layer, facilitated by chloride. This limits the corrosion process by impeding the diffusion of oxygen [41–44], effectively blocking the corrosion process. The high density of the rust layer formed at this concentration indicates its optimal protective effect. The frequency parameter  $|Z|_{0.01\text{Hz}}$ , used to evaluate rust layer protection, also confirms these findings.

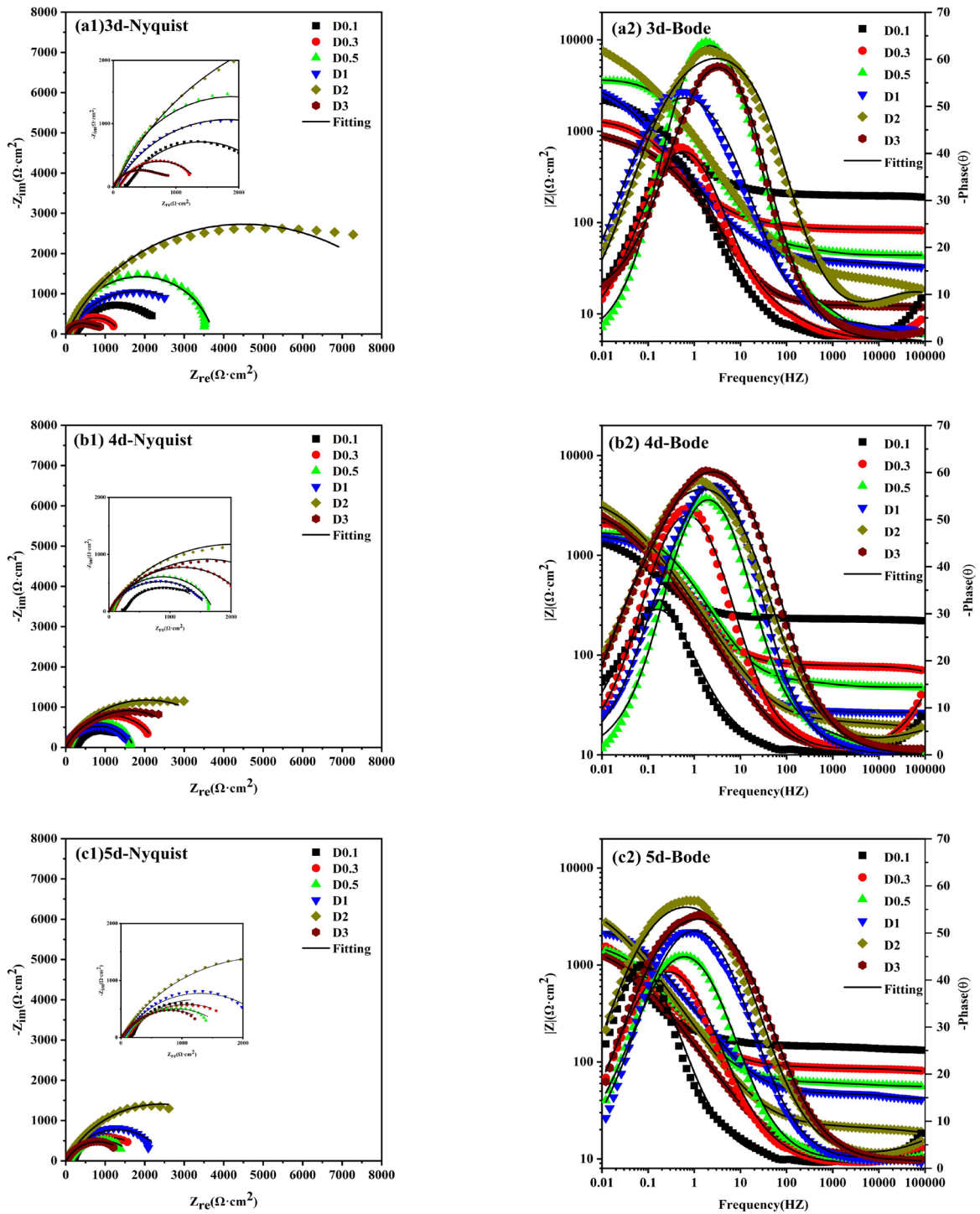


**Figure 20:** EIS results of 17NiCrMo6 steel rust layer after different corrosion time: (a1, a2) 3d, (b1, b2) 4d, (c1, c2) 5d.

In order to study the variation of corrosion current on the surface rust layer of 17NiCrMo6 steel with  $Cl^-$  concentration, SECM surface scanning experiments were conducted, and the test results are shown in Figure 21. According to the principle of electrochemical testing, a smaller local corrosion current on the surface indicates better corrosion resistance of the rust layer. The red and blue color changes in the figure represent the changes in current values. As depicted in the figure, the local feedback current of the rust layer formed under different  $Cl^-$  concentrations varies. Among them, the maximum feedback current of the D0.3 rust layer is  $3.60 \times 10^{-9}$  A, while the minimum feedback current of the D2 rust layer is  $2.30 \times 10^{-9}$  A. This indicates that the rust layer has poor corrosion resistance under D0.3, resulting in a relatively high local corrosion current. At D2 concentration, the rust layer exhibits the best corrosion resistance and the lowest corrosion current.

**Table 5:** Electrochemical parameters after corrosion product film fitting.

TIME (d)	SOLUTION (g/L)	$R_s$ ( $\Omega \cdot \text{cm}^2$ )	$\text{CPE}_1 \cdot 10^{-4}$ ( $\Omega^{-1} \text{cm}^{-2} \text{S}^{-n}$ )	$n_1$	$R_f$ ( $\Omega \cdot \text{cm}^2$ )	$\text{CPE}_2 \cdot 10^{-4}$ ( $\Omega^{-1} \text{cm}^{-2} \text{S}^{-n}$ )	$n_2$	$R_{ct}$ ( $\Omega \cdot \text{cm}^2$ )
3	1	283.3	3.049	0.7765	201.0	8.076	0.6828	2403
	3	83.31	6.796	0.6860	44.83	5.376	0.7390	1270
	5	43.86	0.8586	0.8348	18.33	1.669	0.8423	3675
	10	32.94	1.607	0.6795	7.677	9.163	0.6868	3566
	20	12.37	1.001	0.5261	16.39	2.195	0.7712	9329
	30	11.28	9.370	0.8166	246.9	2.133	0.1298	3843
4	1	291.2	3.956	0.7591	232.7	19.05	0.7031	1380
	3	90.81	2.309	0.7252	78.64	7.663	0.7698	2243
	5	47.55	1.272	0.7943	11.88	3.159	0.8088	1656
	10	26.91	5.840	0.8163	1079	22.04	0.7748	514.1
	20	13.96	1.416	0.3205	22.24	7.208	0.7308	7548
	30	11.29	8.702	0.7606	1699	22.66	0.7695	1274
5	1	262.7	1.437	0.1893	162.9	31.08	0.7353	241
	3	93.22	3.336	0.4483	87.06	16.87	0.6646	2021
	5	54.72	4.855	0.5422	8.470	8.799	0.7455	1754
	10	36.90	3.090	0.9620	4.977	8.005	0.7035	2512
	20	13.47	0.6420	0.3775	22.04	11.72	0.6982	4913
	30	10.14	2.160	0.6756	0.9880	17.20	0.6757	1618

The electrochemical probe scans the surface area of the sample repeatedly at the same interval, which leads to the appearance of a strip-like groove image, as shown in Figure 21. The probe current can reflect the surface morphology of the sample to a certain extent. If there are noticeable defects in the rust layer, the current value in those areas will be significantly higher than elsewhere. As depicted in the figure, the corrosion layer appears relatively dense. However, due to the random nature of the corrosion process, numerous uneven protrusions can be observed in the current distribution. These protrusions represent active points on the surface of the rust layer, indicating that the surface is not flat.

### 3.6. Influence of $\text{Cl}^-$ on the corrosion process of 17NiCrMo6 steel

In general, the corrosion process can be divided into two stages: the initial corrosion stage and the stable corrosion stage. Chloride ions ( $\text{Cl}^-$ ) only play a role in the initial corrosion stage [20]. Once the rust layer has formed, the corrosion rate is determined by the diffusion rate of oxygen ( $\text{O}_2$ ) [45]. This explains why the corrosion rate gradually decreases and stabilizes near a certain value. During the weightlessness experiment, the unique dry and wet cycle mode allows the sample surface to be fully exposed to air for a specific period. This promotes reactions with  $\text{O}_2$ , as illustrated in Figure 22. Iron (Fe) reacts with  $\text{O}_2$  to form  $\text{Fe}(\text{OH})_2$ , which then further oxidizes to form  $\text{Fe}(\text{OH})_3$  and  $\alpha\text{-FeOOH}$ . Eventually,  $\text{Fe}(\text{OH})_3$  dehydrates to form  $\text{Fe}_2\text{O}_3$  and  $\text{Fe}_3\text{O}_4$  [46]. The concentration of  $\text{O}_2$  in the solution is inversely related to the concentration of  $\text{Cl}^-$ . Therefore, higher  $\text{Cl}^-$  concentrations inhibit the complete oxidation of Fe. In the presence of high  $\text{Cl}^-$  concentrations, the initial formation of  $\text{Fe}_3\text{O}_4$  quickly covers the surface, while lower concentrations are more likely to result in the formation of relatively loose FeO and  $\gamma\text{-FeOOH}$ . In summary, increasing  $\text{Cl}^-$  concentration hinders the corrosion impact due to the formation of a dense rust layer, leading to a decrease in weight loss.

The weight loss rates shown in Figure 2 indicate that after eliminating the influence of pure corrosion, the contribution of pure wear and the interaction between wear and corrosion to the weight loss rate of corrosive wear increases with the chloride concentration. Specifically, the weight loss rates for D0.1, D0.3, D0.5, D1, D2, and D3 are 12%, 13%, 11%, 21%, 19%, and 14%, respectively. It is evident that wear only accounts for a small portion of the mass loss caused by corrosive wear, with corrosion being the main contributor. Notably, D2 exhibits the lowest weight loss due to corrosion, and the weight loss due to wear is higher compared to concentrations with faster corrosion rates. This suggests that as the effect of  $\text{Cl}^-$  on corrosion diminishes, its impact on wear becomes more pronounced.

Figure 9 reveals that the outer rust layer of D0.3 contains a significant amount of structurally unstable and loosely bound products such as  $\beta\text{-FeOOH}$  and  $\gamma\text{-FeOOH}$ , which provide poor protection. On the other hand, the corrosion products become denser as the  $\text{Cl}^-$  concentration increases. Similar trends can be observed in the electrochemical properties of the rust layer.  $\text{CPE}_1$  and  $R_f$  represent the behavior of the corrosion product film, while  $\text{CPE}_2$  and  $R_{ct}$  represent the behavior of the double electric layer and corrosion reaction at the solution/

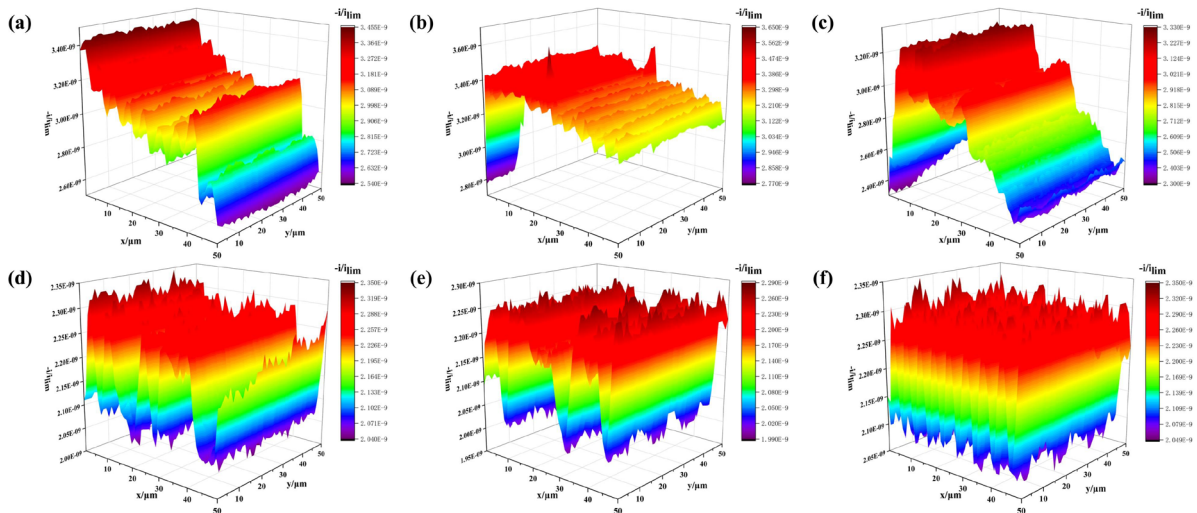


**Figure 21:** Scanning current distribution on the SECM surface of 17NiCrMo6 steel after corrosion of the surface in different concentration corrosion solutions for 5 d in a solution of 0.1 M NaCl + 1 mM FcMeOH: (a) D0.1, (b) D0.3, (c) D0.5, (d) D1, (e) D2, (f) D3.

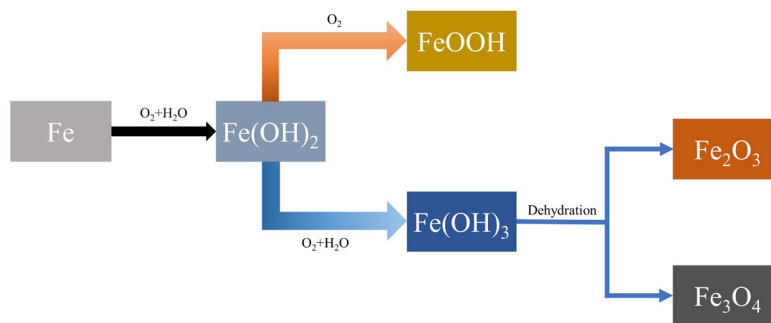


**Figure 22:** Reaction mechanism diagram of corrosion products.

metal interface within the pores of the corrosion product film. Tables 4 and 5 indicate that D2 exhibits a large  $R_f$  in the initial corrosion stage, suggesting that at this concentration, the 17NiCrMo6 steel quickly forms a good protective film. However, over time, the protective effect of the film diminishes, while the charge transfer resistance  $R_{ct}$  increases from  $1337\Omega \cdot \text{cm}^2$  to  $4913\Omega \cdot \text{cm}^2$ . This implies that although the protective effect of the corrosion product film slightly decreases, the inhibition effect of the bimetallic layer structure at the membrane/solution/metal interface on the corrosion reaction strengthens.

From Figure 2 and Table 1, it is evident that the mass loss caused by corrosion and wear alone, as well as the mass loss caused by corrosive wear, are not simply additive. The interaction between corrosion and wear, where corrosion accelerates wear and wear accelerates corrosion, also plays a crucial role in the mass loss [43]. However, as depicted in Figure 1, due to the high hardness and toughness of 17NiCrMo6 steel after heat treatment, wear does not contribute significantly to the mass loss. Instead, the primary factor for mass loss is corrosion, as demonstrated in section 3.2 of the experimental analysis on friction and wear.

### 3.7. The role of Cr, Ni and Mo elements in the inner rust layer

Figure 10 and Figures 12–15 reveal that the elements Cr, Ni, and Mo exhibit varying effects on the inner rust layer at different  $\text{Cl}^-$  concentrations. This aspect requires further discussion in conjunction with the influence of  $\text{Cl}^-$  on corrosion resistance elements. The corrosion mechanism of the rust layer under different  $\text{Cl}^-$  concentrations is depicted in Figure 23.

At low chloride concentrations (D0.1, D0.3, and D0.5), element enrichment is not prominent, except for Cr, which is uniformly dispersed in the inner rust layer. Ni and Mo, on the other hand, aggregate in specific

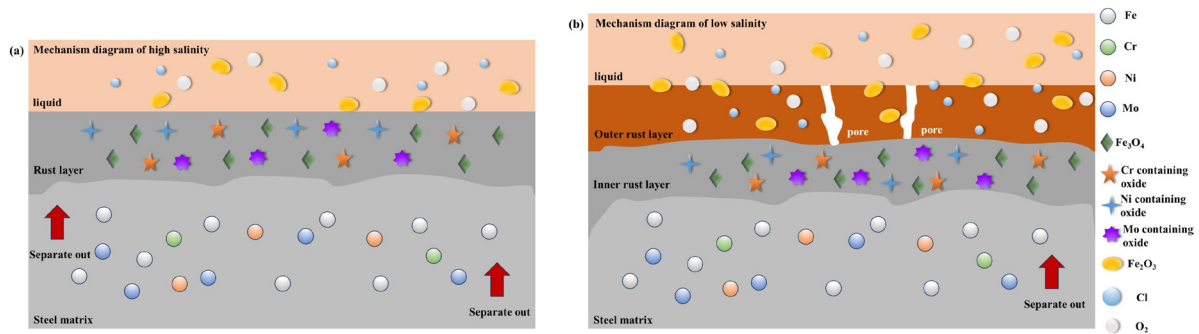


**Figure 23:** Formation mechanism of rust layer under different concentrations: (a) high concentration, (b) low concentration.

positions [47]. At high chloride concentrations (D1, D2, and D3), element enrichment becomes evident, with all elements being evenly dispersed in the inner rust layer. The locations of dispersion for the three elements coincides to a certain extent, indicating their interaction. XPS analysis reveals that the main compounds of Cr in the inner rust layer are  $\text{Cr}(\text{OH})_3$  and  $\text{Cr}_2\text{O}_3$ , while Ni compounds mainly consist of  $\text{NiFe}_2\text{O}_4$  and  $\text{Ni}(\text{OH})_2$ . NiO appears in D0.3 and D1, and Mo compounds primarily include  $\text{MoO}_2$  and  $\text{MoO}_3$ . Due to the electronegativity of  $\text{NiFe}_2\text{O}_4$ , cations such as  $\text{Cr}^{3+}$ ,  $\text{Mo}^{4+}$ , and  $\text{Mo}^{6+}$  are enriched around  $\text{NiFe}_2\text{O}_4$ , thereby impeding the erosion of  $\text{Cl}^-$  on the matrix [41, 48]. Furthermore,  $\text{Cr}(\text{OH})_3$  exhibits a certain anionic selectivity, which also hinders the intrusion of  $\text{Cl}^-$ .

In general, the porosity of the corrosion product film is directly related to the particle size of  $\text{FeOOH}$ . A larger particle size leads to a looser film. Cationic oxides such as  $\text{Cr}^{3+}$ ,  $\text{Mo}^{4+}$ ,  $\text{Mo}^{6+}$ , and  $\text{Ni}^{2+}$  can replace Fe as the attachment point of  $\text{FeOOH}$ . Due to the smaller radius of cations like  $\text{Cr}^{3+}$ ,  $\text{Mo}^{4+}$ ,  $\text{Mo}^{6+}$ , and  $\text{Ni}^{2+}$ , the nucleus radius of  $\text{FeOOH}$  becomes smaller and denser. For example,  $\text{NiFe}_2\text{O}_4$  can increase the amount of nano-sized acicular ferrite and decrease the formation of large-grained acicular ferrite. As the  $\text{Cl}^-$  concentration increases, the corrosion resistant elements become more enriched in the inner rust layer, resulting in smaller particle size of  $\text{FeOOH}$  and a denser rust layer [49]. However, D2, which has the smallest weight loss rate, only has one rust layer due to the accumulation of a large number of corrosion resistant elements in the inner rust layer, effectively blocking the reaction between  $\text{O}_2$  and Fe.

#### 4. CONCLUSIONS

In this study, the corrosive wear mechanism of 17NiCrMo6 steel in different concentrations of desulfurization wastewater was thoroughly investigated, with a focus on the role of Cr, Ni, and Mo. The following conclusions were drawn:

- (1) 17NiCrMo6 steel exhibits a tempered martensite microstructure with high hardness and toughness, where wear contributes negligibly to mass loss and corrosion plays a dominant role.
- (2) In the initial corrosion stage, the high chloride concentration promotes the rapid formation of a protective film on 17NiCrMo6 steel, effectively preventing the initial corrosion. As time progresses, the protective effect of the corrosion product film diminishes, but the corrosion reaction remains more difficult compared to low concentrations. This conclusion is supported by the results of  $R_i$  and  $R_{ct}$ .
- (3) Low chloride concentrations result in the formation of more unstable compounds such as  $\beta\text{-FeOOH}$ ,  $\gamma\text{-FeOOH}$ , and  $\gamma\text{-Fe}_2\text{O}_3$ . On the other hand, high chloride concentrations hinder the diffusion of  $\text{O}_2$ , leading to incomplete oxidation of Fe and the accumulation of corrosion resistant elements in the inner rust layer.
- (4) Corrosion-resistant elements such as Cr, Ni, and Mo enrich the rust layer. At low concentrations, the enrichment is not significant and is only distributed in certain areas. However, as the concentration increases, the enrichment becomes more apparent and is distributed throughout the inner rust layer. The compound synergistic effect of these three elements helps to resist erosion caused by  $\text{Cl}^-$ .

#### 5. BIBLIOGRAPHY

- [1] MENG, Y., LIU, G., HOU, S., *et al.*, "Performance and economic analysis of the cooling tower blowdown water treatment system in a coal-fired power plant", *Chemical Engineering Research & Design*, v. 201, pp. 321–331, Jan. 2024. doi: <http://doi.org/10.1016/j.cherd.2023.11.061>.



- [2] LIN, X.F., ZHONG, T.D., TONG, X.H., *et al.*, “Effect of desulfurization wastewater on slag water system corrosion”, *Chinese Journal of Environmental Engineering*, v. 15, n. 1, pp. 350–359, Jan. 2021.
- [3] ZOU, Y.J., “The application and impact analysis of slurry water treatment system to realize zero discharge of desulfurization waste water”, *Environmental Science Survey*, v. 41, n. 6, pp. 1673–9655, Jun. 2022.
- [4] LIU, X.Y., WU, M., GONG, K., *et al.*, “Stress corrosion cracking behavior on carbon steel under the synergistic effect of chloride and bicarbonate ions in alternating wet-dry environment”, *Corrosion Science*, v. 225, pp. 111624, Dec. 2023. doi: <http://doi.org/10.1016/j.corsci.2023.111624>.
- [5] GOYAL, R., GOYAL, K., “Development of CNT reinforced Al<sub>2</sub>O<sub>3</sub>-TiO<sub>2</sub> coatings for boiler tubes to improve hot corrosion resistance”, *Journal of Electrochemical Science and Engineering*, v. 12, n. 5, pp. 937–945, Aug. 2022. doi: <http://doi.org/10.5599/jese.1291>.
- [6] DONG, B.J., LIU, W., CHEN, L.J., *et al.*, “Unraveling the effect of chloride ion on the corrosion product film of Cr-Ni- containing steel in tropical marine atmospheric environment”, *Corrosion Science*, v. 209, pp. 110741, Dec. 2022. doi: <http://doi.org/10.1016/j.corsci.2022.110741>.
- [7] SAHIL, S.S., GOYAL, K., BHANDARI, D., *et al.*, “Hot corrosion behaviour of thermal-sprayed TiO<sub>2</sub>-reinforced Cr<sub>2</sub>O<sub>3</sub> composite coatings on T-22 boiler steel at elevated temperature”, *Journal of Bio- and Tribo-Corrosion*, v. 7, n. 3, pp. 100, Sep. 2021. doi: <http://doi.org/10.1007/s40735-021-00536-1>.
- [8] SOUSA, J.P., NASCIMENTO, J.M.S., NASCIMENTO, C.C.F., *et al.*, “Corrosion monitoring of low carbon steel in the system with 3% NaCl turbulence: an electrochemical investigation”, *Matéria*, v. 26, n. 3, pp. 13032, May. 2021. doi: <http://doi.org/10.1590/s1517-707620210003.13032>.
- [9] SILVA, F.N., OLIVEIRA, P.M., ARAÚJO, N.M.F.T.S., *et al.*, “Corrosion-cavitation-erosion: surface morphology study of a carbon steel in a multiphase saline bath”, *Matéria*, v. 24, n. 1, pp. 12302, Oct. 2018. doi: <http://doi.org/10.1590/s1517-707620190001.0639>.
- [10] CHEN, J., WANG, J., CHEN, B., *et al.*, “Tribocorrosion behaviors of inconel 625 alloy sliding against 316 steel in seawater Tribology Transactions”, *Tribology Transactions*, v. 54, n. 4, pp. 514–522, Apr. 2011. doi: <http://dx.doi.org/10.1080/10402004.2011.571362>.
- [11] SMITH, F., BROWNLIE, F., HODGKIESS, T., *et al.*, “Effect of salinity on the corrosive wear behaviour of engineering steels in aqueous solutions”, *Wear*, v. 462–463, pp. 203515, Dec. 2020. doi: <http://doi.org/10.1016/j.wear.2020.203515>.
- [12] GAO, B., XU, T., WANG, L., *et al.*, “Achieving a superior combination of tensile properties and corrosion resistance in AISI420 martensitic stainless steel by low-temperature tempering”, *Corrosion Science*, v. 225, pp. 111551, Dec. 2023. doi: <http://doi.org/10.1016/j.corsci.2023.111551>.
- [13] MOU, L.M., BIAN, T.T., ZHANG, S.H., *et al.*, “Understanding the interaction mechanism of chloride ions and carbon dioxide towards corrosion of 3Cr steel”, *Vacuum*, v. 217, pp. 112571, Nov. 2023. doi: <http://doi.org/10.1016/j.vacuum.2023.112571>.
- [14] LI, P., DU, M., “Effect of chloride ion content on pitting corrosion of dispersion-strengthened-high-strength steel”, *Corrosion Communications*, v. 7, pp. 23–34, Sep. 2022. doi: <http://doi.org/10.1016/j.corcom.2022.03.005>.
- [15] PERMEH, S., LAU, K., “Corrosion of galvanized steel in alkaline solution associated with sulfate and chloride ions”, *Construction & Building Materials*, v. 392, pp. 131889, Aug. 2023. doi: <http://doi.org/10.1016/j.conbuildmat.2023.131889>.
- [16] FAN, Y.M., LIU, W., SUN, Z.T., *et al.*, “Effect of chloride ion on corrosion resistance of Ni-advanced weathering steel in simulated tropical marine atmosphere”, *Construction & Building Materials*, v. 266, pp. 120937, Jan. 2021. doi: <http://doi.org/10.1016/j.conbuildmat.2020.120937>.
- [17] WANG, W.Q., YU, Z.F., CUI, Y., *et al.*, “Revealing of corrosion behavior of GH4169 under the alternate environment of intermediate temperature NaCl spraying and marine atmosphere”, *Journal of Materials Research and Technology*, v. 22, pp. 2316–2327, Jan. 2023. doi: <http://doi.org/10.1016/j.jmrt.2022.12.081>.
- [18] XIAO, L.Y., LIU, Q.Q., WANG, J., *et al.*, “Study on corrosion mechanism of Al–Zn coatings in the simulated polluted marine atmosphere”, *Journal of Materials Research and Technology*, v. 25, pp. 6446–6458, Jul. 2023. doi: <http://doi.org/10.1016/j.jmrt.2023.07.091>.
- [19] PENG, C., CAO, G.W., GU, T.Z., *et al.*, “The effect of dry/wet ratios on the corrosion process of the 6061 Al alloy in simulated Nansha marine atmosphere”, *Corrosion Science*, v. 210, pp. 110840, Jan. 2023. doi: <http://doi.org/10.1016/j.corsci.2022.110840>.

- [20] SONG, Y.R., JIANG, G.M., CHEN, Y., *et al.*, “Effects of chloride ions on corrosion of ductile iron and carbon steel in soil environments”, *Scientific Reports*, v. 7, n. 1, pp. 6865, Jul. 2017. doi: <http://doi.org/10.1038/s41598-017-07245-1>. PubMed PMID: 28761066.
- [21] YANG, X.K., ZHANG, L.W., ZHANG, S.Y., *et al.*, “Atmospheric corrosion behaviour and degradation of high-strength bolt in marine and industrial atmosphere environments”, *International Journal of Electrochemical Science*, v. 16, n. 1, pp. 151015, Jan. 2021. doi: <http://doi.org/10.20964/2021.01.68>.
- [22] SUN, M.H., PANG, Y.J., DU, C.W., *et al.*, “Optimization of Mo on the corrosion resistance of Cr-advanced weathering steel designed for tropical marine atmosphere”, *Construction & Building Materials*, v. 302, pp. 124346, Oct. 2021. doi: <http://doi.org/10.1016/j.conbuildmat.2021.124346>.
- [23] ZHAO, Y.G., LIU, W., FAN, Y.M., *et al.*, “Effect of Cr content on the passivation behavior of Cr alloy steel in a CO<sub>2</sub> aqueous environment containing silty sand”, *Corrosion Science*, v. 168, pp. 108591, May. 2020. doi: <http://doi.org/10.1016/j.corsci.2020.108591>.
- [24] SU, W.L., ZOU, J., SUN, L., “Effects of nano-alumina on mechanical properties and wear resistance of WC-8Co cemented carbide by spark plasma sintering”, *International Journal of Refractory & Hard Metals*, v. 92, pp. 105337, Nov. 2020. doi: <http://doi.org/10.1016/j.ijrmhm.2020.105337>.
- [25] FAN, Y.M., LIU, W., LI, S.M., *et al.*, “Evolution of rust layers on carbon steel and weathering steel in high humidity and heat marine atmospheric corrosion”, *Journal of Materials Science and Technology*, v. 39, pp. 190–199, Feb. 2020. doi: <http://doi.org/10.1016/j.jmst.2019.07.054>.
- [26] WANG, M.N., QIAO, C., JIANG, X.L., *et al.*, “Microstructure induced galvanic corrosion evolution of SAC305 solder alloys in simulated marine atmosphere”, *Journal of Materials Science and Technology*, v. 51, pp. 40–53, Aug. 2020. doi: <http://doi.org/10.1016/j.jmst.2020.03.024>.
- [27] WANG, L.B., WANG, J.H., HU, W.B., “Influence of Cl<sup>-</sup> on the initial corrosion of weathering steel in simulated marine-industrial atmosphere”, *International Journal of Electrochemical Science*, v. 13, n. 8, pp. 7356–7369, Aug. 2018. doi: <http://doi.org/10.20964/2018.08.19>.
- [28] ZHANG, X.X., GAO, Z.M., XIU, Y., *et al.*, “Image analysis of synthesized corrosion products applied to in-situ analysis of Q235 steel under simulated marine atmosphere”, *International Journal of Electrochemical Science*, v. 14, n. 2, pp. 1713–1724, Feb. 2019. doi: <http://doi.org/10.20964/2019.02.76>.
- [29] WU, W., CHENG, X.Q., ZHAO, J.B., *et al.*, “Benefit of the corrosion product film formed on a new weathering steel containing 3% nickel under marine atmosphere in Maldives”, *Corrosion Science*, v. 165, pp. 108416, Apr. 2020. doi: <http://doi.org/10.1016/j.corsci.2019.108416>.
- [30] WU, W., DAI, Z.Y., LIU, Z.Y., *et al.*, “Synergy of Cu and Sb to enhance the resistance of 3%Ni weathering steel to marine atmospheric corrosion”, *Corrosion Science*, v. 183, pp. 109353, May. 2021. doi: <http://doi.org/10.1016/j.corsci.2021.109353>.
- [31] SUN, M.H., YANG, X.J., DU, C.W., *et al.*, “Distinct beneficial effect of Sn on the corrosion resistance of Cr–Mo low alloy steel”, *Journal of Materials Science and Technology*, v. 81, pp. 175–189, Aug. 2021. doi: <http://doi.org/10.1016/j.jmst.2020.12.014>.
- [32] ZHAO, Q.H., LIU, W., ZHU, Y.C., *et al.*, “Effect of small content of chromium on wet-dry acid corrosion behavior of low alloy steel”, *Acta Metallurgica Sinica*, v. 30, n. 2, pp. 164–175, Feb. 2017. doi: <http://doi.org/10.1007/s40195-016-0513-z>.
- [33] HAO, L., ZHANG, S.X., DONG, J.H., *et al.*, “Atmospheric corrosion resistance of MnCuP weathering steel in simulated environments”, *Corrosion Science*, v. 53, n. 12, pp. 4187–4192, Dec. 2011. doi: <http://doi.org/10.1016/j.corsci.2011.08.028>.
- [34] LIU, W.M., LIU, J., PAN, H.B., *et al.*, “Synergistic effect of Mn, Cu, P with Cr content on the corrosion behavior of weathering steel as a train under the simulated industrial atmosphere”, *Journal of Alloys and Compounds*, v. 834, pp. 155095, Sep. 2020. doi: <http://doi.org/10.1016/j.jallcom.2020.155095>.
- [35] WANG, Y.M., YANG, Y.H., QU, J.L., *et al.*, “Effect of oxide layer on the electrochemical corrosion behavior of a Ni-based superalloy in 3.5 wt% NaCl”, *International Journal of Electrochemical Science*, v. 18, n. 10, pp. 100310, Oct. 2023. doi: <http://doi.org/10.1016/j.ijoes.2023.100310>.
- [36] XIE, R.Z., GENG, R.C., ZHANG, Q., *et al.*, “Investigation of Q235 steel electrochemical corrosion behavior in naturally dried sandy soil”, *International Journal of Electrochemical Science*, v. 18, n. 12, pp. 100376, Dec. 2023. doi: <http://doi.org/10.1016/j.ijoes.2023.100376>.
- [37] ZHAO, S.C., JING, Y.Y., LIU, T., *et al.*, “Corrosion behavior and mechanism of carbon steel in industrial circulating cooling water system operated by electrochemical descaling technology”, *Journal of Cleaner Production*, v. 434, pp. 139817, Jan. 2024. doi: <http://doi.org/10.1016/j.jclepro.2023.139817>.

- [38] JIANG, P., LENG, J.H., LIAO, K.X., *et al.*, “Investigation into the mechano-electrochemical interaction of internal and external corrosion defects on pipe surfaces”, *International Journal of Pressure Vessels and Piping*, v. 207, pp. 105098, Feb. 2024. doi: <http://doi.org/10.1016/j.ijpvp.2023.105098>.
- [39] YE, Z.X., GUAN, L., LI, Y., *et al.*, “Understanding the galvanic corrosion of Cu-Ni alloy/2205 DSS couple using electrochemical noise and microelectrochemical studies”, *Corrosion Science*, v. 224, pp. 111512, Nov. 2023. doi: <http://doi.org/10.1016/j.corsci.2023.111512>.
- [40] ZHANG, S., LIU, J., TANG, M., *et al.*, “Role of rare earth elements on the improvement of corrosion resistance of micro-alloyed steels in 3.5 wt.% NaCl solution”, *Journal of Materials Research and Technology*, v. 11, pp. 519–534, Mar. 2021. doi: <http://doi.org/10.1016/j.jmrt.2021.01.041>.
- [41] LI, G., WU, W., CHAI, P.L., *et al.*, “Influence of Cr and Ni elements on the electrochemical and early corrosion behavior of FeMnAlC low-density steel”, *Journal of Materials Research and Technology*, v. 23, pp. 5892–5906, Mar. 2023. doi: <http://doi.org/10.1016/j.jmrt.2023.02.219>.
- [42] CALDERÓN-HERNÁNDEZ, J.W., GONZÁLEZ-RAMÍREZ, M.F., SEPULVEDA-CASTAÑO, J.M., *et al.*, “Electrochemical characterization of 13Cr low-carbon martensitic stainless steel – corrosion study with a mini-cell setup”, *Journal of Materials Research and Technology*, v. 21, pp. 2989–2998, Nov. 2022. doi: <http://doi.org/10.1016/j.jmrt.2022.10.094>.
- [43] MA, Y., YUAN, D.W., HAN, C., “Electrochemical corrosion behaviour of carbon steel reinforcement in metakaolin-limestone modified concrete exposed to simulated soil solution”, *International Journal of Electrochemical Science*, v. 16, n. 5, pp. 210518, May. 2021. doi: <http://doi.org/10.20964/2021.05.23>.
- [44] SHI, S.H., XIONG, Y.Q., “Electrochemical Corrosion Resistance of Carbon Steel Rebar in Concrete Structures Exposed to 3.5wt% NaCl Solution: ‘Effect of Green Inhibitors and Micro-Silica as Partial Replacement’”, *International Journal of Electrochemical Science*, v. 16, n. 5, pp. 210527, May. 2021. doi: <http://doi.org/10.20964/2021.05.24>.
- [45] GENG, Z., YAO, N., ZHOU, X.C., *et al.*, “Understanding the intrinsic effect of fly ash on passivity and chloride-induced corrosion of carbon steel and stainless steel in cement extract solutions”, *Cement and Concrete Composites*, v. 143, pp. 105236, Oct. 2023. doi: <http://doi.org/10.1016/j.cemconcomp.2023.105236>.
- [46] ZHANG, T.Y., LIU, W., CHEN, L.J., *et al.*, “On how the corrosion behavior and the functions of Cu, Ni and Mo of the weathering steel in environments with different NaCl concentrations”, *Corrosion Science*, v. 192, pp. 109851, Nov. 2021. doi: <http://doi.org/10.1016/j.corsci.2021.109851>.
- [47] WEI, A., FENG, Y.J., WU, L.Y., *et al.*, “Corrosion wear behavior of 30CrNi<sub>2</sub>MoVA steel in simulated seawater”, *Materials Letters*, v. 349, pp. 134750, Oct. 2023. doi: <http://doi.org/10.1016/j.matlet.2023.134750>.
- [48] HAO, L., ZHANG, S.X., DONG, J.H., *et al.*, “A study of the evolution of rust on Mo–Cu-bearing fire-resistant steel submitted to simulated atmospheric corrosion”, *Corrosion Science*, v. 54, pp. 244–250, Oct. 2012. doi: <http://doi.org/10.1016/j.corsci.2011.09.023>.
- [49] CANO, H., NEFF, D., MORCILLO, M., *et al.*, “Characterization of corrosion products formed on Ni 2.4 wt%–Cu 0.5 wt%–Cr 0.5 wt% weathering steel exposed in marine atmospheres”, *Corrosion Science*, v. 87, pp. 438–451, Oct. 2014. doi: <http://doi.org/10.1016/j.corsci.2014.07.011>.